Influence of friction stir welding on the localised corrosion behaviour of AA2060 T8E30 and AA2099 T83 Al-Li alloys

Garg, Vishant; van Dam, Joost P.B.; Michailidou, Emmanouela; Gonzalez-Garcia, Yaiza

DOI
10.1016/j.corsci.2024.112519

Publication date
2024

Document Version
Final published version

Published in
Corrosion Science

Corrosion Science 241 (2024) 112519

Contents lists available at ScienceDirect

Corrosion Science

journal homepage: www.elsevier.com/locate/corsci

Influence of friction stir welding on the localised corrosion behaviour of AA2060 T8E30 and AA2099 T83 Al-Li alloys

Vishant Garg, Joost P.B. van Dam, Emmanouela Michailidou, Yaiza Gonzalez-Garcia *

Delft University of Technology, Department of Materials Science and Engineering, Mekelweg 2, Delft 2628CD, the Netherlands

ARTICLE INFO

Keywords:
A: Aluminium-lithium alloys
B: In-situ time lapse imaging
B: Potentiodynamic polarisation
C: Friction Stir Welding
C: Localised corrosion

ABSTRACT

The effect of friction stir welding (FSW) on the microstructure and localised corrosion behaviour of the dissimilar weld of AA2099 T83 and AA2060 T8E30 alloys is investigated. FSW results in a drastic change in the microstructure thus altering their corrosion behaviour. The heat-affected region exhibits similar attack morphology to their respective base metal but is the most protected region. The stir zone (SZ) is the most susceptible to attack. During immersion of the entire weld, attack initiation occurs from the AA2060 SZ due to galvanic activity within the region caused by the overlap of the grains in the weld zone.

1. Introduction

The use of aluminium alloys has steadily increased in the last few decades due to their advantages such as being lightweight, high corrosion resistance, and having very good thermal and electrical conductivity [1–4]. One of the most widely used aluminium alloys in aircraft manufacturing is the AA2024 T3 alloy, a high-strength and lightweight alloy [5,6]. The new third-generation aluminium-lithium (Al-Li) alloys, such as the AA2099 and AA2060 alloys which have a lithium content of less than 2 %, are considered as possible candidates to replace the AA2024 alloy in aerospace structures, due to their highly desirable combination of mechanical properties [7–9].

The AA2099 alloy has been found to save up to 14 % weight on major structural components of the aircraft wings. In addition, the AA2099 alloy exhibits higher transverse ductility (6 % increase), excellent stress corrosion cracking resistance, and toughness compared to its predecessor in the 2nd generation (AA2090 alloy) [10]. The AA2060 alloy also provides exceptional mechanical properties such as high stiffness (20 % higher than AA2024 T3) and high strength-to-weight ratio (25 % higher than AA2024 T3). It has been specifically developed for aerospace components such as the fuselage panels, and upper and lower wing structures of jetliners due to its low density [9,11,12].

Despite their numerous advantages, these Al-Li alloys are susceptible to localised forms of corrosion, which has been associated with the high reactivity of Li and the resultant Li-containing intermetallic phases [13]. The T_1 (Al_2CuLi) phase particles are the primary strengthening phase and dictate the strength level of the Al-Li alloy [14]. Although the T_1 phase is very beneficial for the mechanical properties of Al-Li alloys [15,16], the effect it has on the corrosion behaviour of the alloy is still controversial. Buchheit et al. [16] determined that the T_1 precipitate is highly active compared to the matrix, resulting in local galvanic cells around these particles in a corrosive environment.

Friction stir welding (FSW) is a solid-state welding technique which produces high-integrity joints in difficult to weld materials such as aluminium, copper, and magnesium [17]. During FSW, the alloys undergo heavy plastic deformation, heat cycles, and recrystallization which causes numerous microstructural changes such as grain growth and refinement, local compositional changes and added impurities. Unlike other welding methods, such as tungsten inert gas (TIG) welding or laser welding, FSW does not lead to metal fusion since the temperatures used for joining are slightly below the melting point of the metal or alloy [18]. FSW leads to four characteristic zones in the joined samples: the stir zone (SZ), the thermo-mechanically affected zone (TMAZ), the heat-affected zone (HAZ), and the base metal (BM) [17,19,20]. The microstructural differences between the various zones in the friction welded joint and the presence of various intermetallic particles in them can alter the electrochemical behaviour of the individual zones and induce preferential corrosion susceptibilities or galvanically enhanced dissolution of active regions [21,22]. Due to their metallurgical complexity, the corrosion susceptibilities of these Al-Li alloys friction stir weldments are unpredictable. Cai et al. [1] proposed that during welding of the AA2060 alloy, the heat generated promotes the dissolution of the T_1 phase particles, while the stirring motion of the tool causes fragmentation and re-distribution of the coarse particles in the SZ and

* Corresponding author.
E-mail address: y.gonzalezgarcia@tudelft.nl (Y. Gonzalez-Garcia).

https://doi.org/10.1016/j.corsci.2024.112519
Received 5 June 2024; Received in revised form 9 October 2024; Accepted 15 October 2024
Available online 19 October 2024

TMAZ. This was also concluded by Donatus et al. [23] in their work on the FSW of AA2198 alloy.

Current literature on FSW of Al alloys and especially Al-Li alloys is predominantly limited to welding a single alloy [1,3,23–33]. The welding of dissimilar alloys and their electrochemical behaviour presents a substantially complex scenario due to the different chemical compositions of the alloys and the formation of a mixed stir zone of the two alloys. Bertoncello et al. [34] observed that the boundaries of the mixed stir zone of dissimilar welds present defects related to the welding process such as cold hooks, where the two alloys are not joined properly. These defects can cause failure of the weld joint since they are sites for nucleation of fatigue cracks. Meanwhile, Fattah-alhosseini et al. [35] observed that the transition between the two alloys in the mixed stir zone of the weld is rather apparent, which allowed them to discriminate the layers of each alloy in the stir zone. Additionally, they found that FSW led to grain refinement and the breakdown/dissolution of intermetallic particles in the SZ.

It has been suggested that FSW of dissimilar alloys leads to a joint region that is not necessarily superior to its parent alloys, but rather exhibits middling properties with regard to its electrochemical behaviour [35]. However, the weld region is usually more susceptible to localized corrosion compared to the base material due to the coarsening and dissolution of intermetallic particles and precipitates [34–36]. These factors have been reported to play a major effect in the changes in the corrosion behaviour of the weld zones. Nevertheless, there is a lack of research on the FSW of dissimilar aluminium-lithium alloys. Therefore, it is of utmost importance to investigate the corrosion behaviour of dissimilar weld joints of such Al-Li alloys, especially their mixed stir zone, if they ever replace the current generation of Al alloys.

The present work aims to investigate the effect of friction stir welding on the microstructure of aluminium-lithium alloys - AA2060 T8E30 and AA2099 T83, and to subsequently study the electrochemical response of the individual weld zones and the entire weld in saline aqueous conditions. The combination of AA2060 T8E30 and AA2099 T83 alloys welded by FSW in a lap configuration was selected for this work since these alloys are potential candidates for their application as skin and stringer in the fuselage panels of airplanes. Microstructural characterisation of the weld zones was performed using scanning electron microscopy (SEM) and optical microscopic techniques to investigate the differences between the weld zones. Electrochemical tests – open circuit potential (OCP), linear polarisation resistance (LPR), and potentiodynamic polarisation were carried out locally in individual weld zones to determine the corrosion behaviour and quantify the corrosion kinetics of each region. The role of intermetallic particles on the corrosion behaviour and the morphology of the corrosion attack and its evolution with time was investigated by in-situ time-lapse imaging during immersion of the individual weld zones. Finally, the performance of the entire weld in a corrosive environment was evaluated using scanning Kelvin probe (SKP) to map the surface potential of the weld along with in-situ time-lapse imaging during immersion of the entire weld joint.

2. Experimental

2.1. Materials

Commercially produced friction stir welded samples of Z-shaped extrusion of AA2099 T83 alloy and a cold-rolled sheet of AA2060 T8E30 alloy were provided by LORTEK Technological Centre (Ordizia, Spain). The chemical composition of both alloys is given in Table 1.

A rotational speed of 1200 rpm and a 250 mm/min welding speed in force control mode with an axial force of 6.25 kN was applied to weld the sample using friction stir welding [37].

2.2. Sample preparation

Sections of the sample were cut perpendicular to the welding direction to obtain cross-sectional samples of the entire welded region in 4.5 mm×23.5 mm rectangular coupons. The samples were mechanically grinded from 180 – 4000 grit using silicon-carbide abrasive papers and distilled water as a lubricant. This was followed by polishing using 3 μm and 1 μm diamond pastes to obtain a mirror finish surface. The samples were then rinsed with distilled water, followed by ethanol and dried using filtered compressed air.

2.3. Microstructure evaluation

The samples were etched to perform the microstructural evaluation using Keller's reagent (1 mL HF + 2.5 mL HNO_3 + 1.5 mL HCl + 95 mL H_2O) for 10 seconds. Etched samples were rinsed using distilled water, followed by ethanol and dried using filtered compressed air. Microstructural characterisation was performed using a Keyence VHX 5000 digital microscope, Leica DM-LM optical microscope, and JEOL JSM IT100 Scanning Electron Microscopy (SEM) fitted with Energy Dispersive X-ray Spectroscopy (EDS) to evaluate the elemental analysis of the specimen. The cross-sectional SEM surface characterisation of the weld zones was performed at 5 kV, collecting backscattered electrons. The EDS spectra were analysed using the JEOL software of the SEM-EDS system, while the optical micrographs were analysed using ImageJ, and SEM images using Adobe Photoshop CC 2019.

To obtain the average grain area within each weld zone of the alloys, 15 grains in each zone were selected at random and their area was calculated using Adobe Photoshop CC 2019. The mean value of these measurements was then tabulated along with their standard error. The distribution (population) density of intermetallic particles and their average area were also obtained using Adobe Photoshop. To determine this, the colour range and contrast of each type of particle was selected within the SEM micrographs. Next, the threshold was adjusted to ensure that the selection was not affected by the brightness of the image. Finally, the images were analysed by the software to ascertain the distribution density (area % of coverage) of the particles and the average area (μm^2) of the intermetallic particles.

2.4. Micro-hardness testing

Vickers micro-hardness measurements were carried out using a Struers DuraScan micro-hardness testing machine with a load of 0.5 kgF and a dwell time of 10 s. An edge distance of 0.5 mm and a distance of 10 D (diameter of the tip) was maintained between every two consecutive indentations. Experiments were repeated two additional times to ensure the reproducibility of the results. The mean of the recorded measurements was calculated with the standard deviation and standard error.

Table 1
Chemical composition of the AA2060 T8E30 and AA2099 T83 alloys [37].

	Chemical Composition (wt%) of the AA2060 T8E30 and AA2099 T83 alloys									
	Si	Fe	Cu	Mn	Mg	Zn	Ti	Ag	Li	Zr
AA2060 T8E30	0.07	0.07	3.4–4.5	0.1–0.5	0.6–1.1	0.3–0.5	0.1	0.05–0.5	0.6–0.9	0.05–0.15
AA2099 T83	0.05	0.07	2.4–3.0	0.1–0.5	0.1–0.5	0.4–1	0.1	-	1.6–2.0	0.05–0.12
Aluminium: Remainder										

2.5. Electrochemical measurements

The electrochemical experiments were conducted in a 3-electrode electrochemical cell using a Biologic VSP-300 Potentiostat and EC-lab collection software. The sample was used as the working electrode, a platinum plate mesh as a counter electrode, and an Ag/AgCl (saturated KCl) reference electrode. All experiments were conducted in a freshly prepared 0.1 M NaCl aqueous solution of near-neutral pH in aerated conditions at room temperature. Experiments were repeated threefold to confirm the reproducibility of the results. Samples were masked using a 90 μm thick extruded PTFE 5490 tape (3 M Ltd) on which a 1 mm diameter opening was made using a biopsy needle to isolate an exposed area of 0.008 cm^2. The working electrode was connected to the potentiostat using copper adhesive tape (3 M Ltd). Since the TMAZ regions in both alloys are very narrow, less than 0.5 mm in width, experiments were not performed for this region as the zone did not fall within the resolution of the experimental apparatus and could not be isolated.

The open-circuit potential (OCP) and linear polarisation resistance (LPR) were monitored over a period of 24 h. OCP was measured for 1-h intervals, after which the LPR was measured with a sweep rate of 0.167 mV/s at ±10 mV versus OCP. Potentiodynamic polarisation tests were performed by linear sweep voltammetry. Anodic and cathodic polarisation curves were recorded separately. Samples were kept at OCP condition for 2 h prior to polarisation to reach steady state. A sweep rate of 0.167 mV/s was applied between –0.05 and +1 V vs OCP for anodic polarisation, and between +0.05 and –1 V vs OCP for cathodic polarisation. Tafel extrapolation was performed using the EC-lab software to obtain the corrosion potential (E_{corr}) and the corrosion current density (i_{corr}) of the sample using the Stern equation.

2.6. In-situ time-lapse immersion tests

The in-situ time-lapse imaging during immersion was based on the approach by Sullivan et al. to reveal localised corrosion mechanisms and preferential phase attacks in the microstructure of the sample [38]. Tests were carried out over a period of 24 h in a freshly prepared 0.1 M NaCl aqueous solution of near-neutral pH at room temperature.

For the immersion test on individual weld regions of the alloys, the polished and etched samples were masked with 90 μm thick extruded PTFE 5490 tape (3 M Ltd) in which a defect of 0.5 mm diameter was made using a biopsy needle to isolate an exposed area of 0.002 cm^2. The samples were then secured inside a petri dish using an arrangement of double-sided tape and PTFE tape. An optical microscope (Leica DM-LM) fitted with a Lumenera Infinity I camera was used to observe the sample and record digital images. A submersible cap with a thin microscopic glass window was used as a protective cover for the objective lens to prevent contamination and damage. The petri dish was filled with 250 mL of freshly prepared 0.1 M aqueous NaCl and the optical focus under the objective lens/camera was adjusted to obtain clear in-situ images of the exposed sample area. The in-situ time-lapse immersion tests were not performed on the TMAZ regions of the alloys since they could not be individually isolated due to their extremely narrow width.

For the immersion test on the entire weld region of the alloys, the polished sample was secured inside a petri dish using a similar arrangement of double-sided and PTFE tapes. A high-resolution camera (12 megapixels), mounted on a tripod stand, was used to observe the sample and record digital images. The petri dish containing the sample was then placed under the microscope/camera and was filled with 250 mL of freshly prepared 0.1 M NaCl solution as the electrolyte. Digital images were taken using the Infinity Analyze software at 1-min intervals for 24 h using the time-lapse function of the camera. After the end of the experiment, at 24 h, the samples were de-smutted in a solution of 30 % HNO_3 for 15 s to remove the corrosion products from the surface. The de-smutting process was limited to 15 s to avoid any added corrosion attack or microstructural changes to the surface. The de-smutted samples were then studied under SEM at 5 kV collecting emitted secondary electrons.

2.7. Scanning Kelvin Probe (SKP)

SKP measurements were carried out using a KP Technology SKP 5050 system with a relative humidity chamber. The SKP was operated using a gold probe tip with a 0.5 mm circular flat end. The probe was set to vibrate at a frequency of 65 Hz with an amplitude of 40 μm. Measurements were taken using a sample backing voltage, V_B, in the range of ± 6600 mV. Prior to each experiment, the probe was calibrated to avoid a potential shift of the probe. The measured electrode potentials are in reference to the standard hydrogen electrode (SHE) after calibration against $Cu/CuSO_4$ (0.316 V vs SHE) [39].

The polished sample was taken and 1 mL of freshly prepared 0.1 M NaCl solution was applied on the surface of the sample. Once the moisture evaporated under ambient conditions, a thin homogeneous film of salt was formed on the surface of the sample. The sample was then placed on the stage in the relative humidity chamber. The RH was set to 93 % at room temperature (21°C) and allowed to stabilise. The moisture in the chamber rehydrated the salt crystals on the surface thus creating a film and behaving as an electrolyte. The total area to be scanned was 16.3 mm×3.3 mm mapped at a step size of 0.317 μm. The distance between tip and surface was kept constant by using the gradient constant function.

3. Results and discussion

3.1. Microstructure analysis of the FSW Al-Li alloys

The cross-sectional sample of the weld joint is shown in Fig. 1a. The extruded AA2099 alloy is located on the top, whereas the cold-rolled sheet AA2060 alloy is located at the bottom. The alloys were welded using FSW, resulting in the formation of different zones due to the deformation and thermal cycle each region undergoes. Fig. 1b shows the entire weld joint of the alloys corresponding to the boxed area from Fig. 1a.

An irregular basin shape is observed in the weld centre, which represents the stir zone (SZ) of the welded alloys. The SZ is formed due to recrystallisation caused by severe plastic deformation and high temperatures during welding [18]. It is the region that roughly corresponds to the path of the pin during FSW [17]. The region towards the bottom of the SZ, encircled in Fig. 1a and Fig. 1b, corresponds to the joined region of both alloys and is referred to as the weld nugget. As the temperatures in FSW are insufficient for metal fusion [18], an overlapping of the alloys is observed here (Fig. 1b), indicating that this region (AA2060 SZ) consists of alloying elements from both alloys, thus forming a banded structure. This effect has also been observed in friction stir weldments of other dissimilar aluminium alloys [34,35,40,41].

Next to the SZ, a narrow region of less than 0.5 mm in width surrounds it in both alloys. This region is known as the thermo-mechanically affected zone (TMAZ). This zone, too, undergoes deformation and thermal cycles during welding. However, the strain and temperature experienced by this region are lower than those of the SZ. Numerical simulations by finite element analysis have shown that the temperatures in the TMAZ regions are approximately 22 % lower than that of the SZ [18]. Therefore, the TMAZ retains the microstructure of the base metals even after distortion of the grains induced by the severe stirring motion of the tool pin [31]. The heat-affected zone (HAZ) lies next to the TMAZ regions, as seen in Fig. 1b. This region does not undergo plastic deformation, and the temperatures during welding are much lower here than in the SZ (50–55 % lower) and the TMAZ (30–32 % lower) [17,18]. The base metal (BM) is the region unaffected by the welding process and is located on either end of the weld sample.

The Vickers micro-hardness values were measured along the entire weld joint cross-section for both alloys, as seen in Fig. 1b, indicated by row 1 (red line) for the AA2099 alloy and row 2 (yellow line) for the

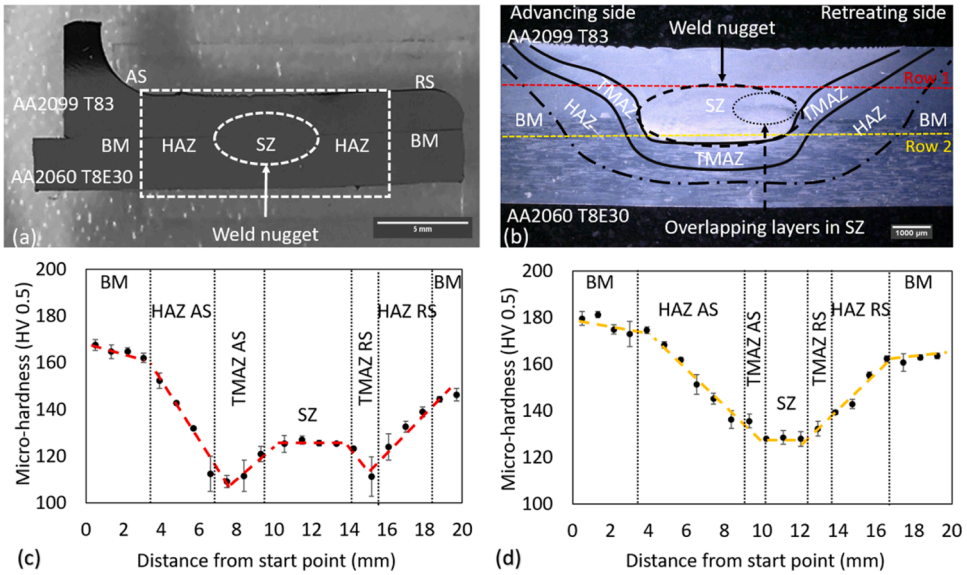

Fig. 1. (a): Optical image of cross-sectional sample of the FSW AA2099 and AA2060 alloys, (b): Optical micrograph of the weld joint showing the respective weld zones in both alloys, (c): Microhardness profile of the AA2099 alloy weld joint (Row 1 – red line), and (d): Microhardness profile of the AA2060 alloy weld joint (Row 2 – yellow line).

AA2060 alloy weld regions. The respective micro-hardness profiles are shown in Fig. 1c and 1d. The highest hardness values in the two profiles are observed for the base metal of both alloys, 167 ± 2 HV for the AA2099 BM and 181 ± 3 HV for the AA2060 BM. It has been found that the hardness of the alloys stems from the production and strengthening methods, such as extrusion for the AA2099 alloy and cold rolling for the AA2060 alloy [42–44].

The AA2099 alloy weld section exhibits an irregular W-shaped micro-hardness profile (Fig. 1c). This irregular W-shaped profile has also been observed for the weldments of other friction stir welded Al alloys [31,32,45], thus demonstrating that the hardness profile is related to the geometry of the weld. The AA2060 alloy, on the other hand, presents an irregular V-shaped micro-hardness profile across its weldment, as observed in Fig. 1d. For both alloys, the micro-hardness decreases towards the centre of the weld joint. In the AA2060 alloy, the lowest microhardness corresponds to the SZ region of the alloy at 128 ± 1 HV. However, for the AA2099 T8E30 alloy, the lowest microhardness of 109 ± 3 HV is observed at the HAZ-TMAZ interface, whereas the SZ of this alloy exhibits higher hardness values (125 ± 4 HV). This phenomenon has been reported by other researchers as well for the FSW of Al-Li alloys and is discussed later on [23,41].

The typical microstructure of the various weld zones (BM, HAZ, and SZ) of the AA2060 and AA2099 alloys, observed by SEM, are shown in Fig. 2(a-c) and (d-f), respectively. The BM of the AA2060 alloy has extremely large and flat grains, shown and marked in Fig. 2a (black outline), with an average grain area of 52792 ± 12491 μm^2, formed due to the cold rolling process [43]. The average grain area of the weld zones for both alloys, determined by image analysis of the SEM micrographs in Fig. 2, are compiled in Fig. 3. The coarse constituent particles were identified as the bright spots on the surface (yellow circles) due to the heavier elements in them compared to the alloy matrix. An EDS point scan revealed that these particles were Cu-rich intermetallics with either Mg or traces of Mn and Fe. It is suggested that these coarse particles in the AA2060 alloy could be the S′ phase (Al_2CuMg) particles and the Al-Cu-Fe-Mn intermetallic particles [1,12,45].

The dark particles observed on the surface (Fig. 2) were assumed to be dispersoids and/or hardening precipitates in the alloy given their dimensions and locations [1,45–47]. Since these particles usually are very small in size, in the order of nanometre for the hardening precipitates and nano–micrometre range for dispersoids, they could not be characterised with the current apparatus. Additionally, lithium cannot be detected by EDS due to its very low energy of characteristic radiation (Z=3), which further restricts the analysis. It is known that hardening precipitates are mostly pinned to the dislocation sites and grain boundaries, whereas the dispersoids are homogeneously distributed in the alloy [46,48]. For the case of AA2060, the hardening precipitates reported in the literature are the T_1 (Al_2CuLi), δ′ (Al_3Li), and θ′ (Al_2Cu) particles, while the dispersoids present are the β′ (Al_3Zr) phase articles [1,45,48,49].

Fig. 4 presents the distribution (population) density of the intermetallic particles in the weld zones of each alloy, while Fig. 5 compiles the average size of the intermetallic particles within the weld zones. These results were obtained by image analysis of the SEM micrographs by considering the contrast of the images, i.e. bright particles represent coarse constituent particles and dark spots represent dispersoids and hardening precipitates [23,46,50]. While we could not differentiate between the hardening precipitates and dispersoids from image analysis of the SEM micrographs, we have used the microhardness measurements from Fig. 1(c, d) to complement our analysis. Previous investigations have established that the distribution of hardening precipitates, such as T_1 and S′, in the zones of a welded sample can be directly related to the microhardness measurements along the weld profile [21,23,29,32,36], i.e. lower microhardness corresponds to lower distribution of the hardening precipitates.

Fig. 2d shows the typical microstructure of the AA2099 alloy base metal with much smaller grains, with an average grain area of 46 ± 11 μm^2. These refined grains are formed due to recrystallisation of the grains during hot extrusion of the alloy [42]. The coarse constituent particles were found to be Al-Cu-Fe-Mn particles of both low and high Cu content. Ma et al. [46] suggested that these particles with different Cu content were formed during the production processes of the AA2099 alloy and revealed that they exhibit different electrochemical behaviour from each other. A higher distribution density (population) of hardening precipitates and/or dispersoids is observed in the AA2099 alloy (~30 %) as compared to the AA2060 alloy (Fig. 4(b)). Based on the literature, the precipitates that are usually present in this alloy are the T_1, δ′, and θ′ particles [9,42,46,50–53]. In contrast, the dispersoids present are mostly β′ phase particles and Al-Cu-Mn-Li intermetallic particles [42,46,50–52,54].

The HAZ of AA2060 and AA2099 alloys are seen in Fig. 2b and 2e,

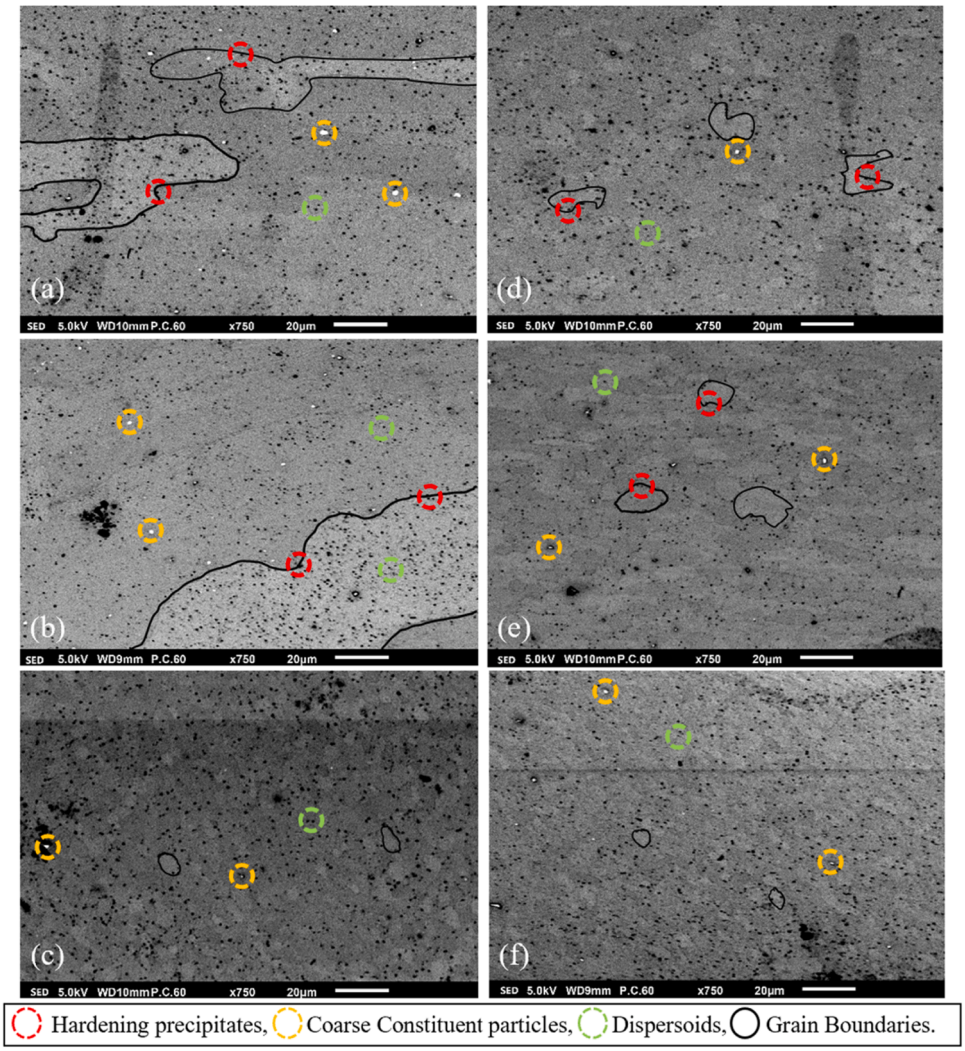

Fig. 2. Typical microstructure of the weld zones observed under SEM for AA2060 alloy: (a) BM, (b) HAZ, (c) SZ, and AA2099 alloy: (d) BM, (e) HAZ, (f) SZ. The coloured circles highlight a few examples of the intermetallic particles in the alloy matrix. The hardening precipitates are selected at/near the grain boundaries and the dispersoids are selected inside the grains.

respectively. The grains of this region are much smaller compared to the BM, with a 60 % reduction for the advancing side (AS) and a 65 % reduction for the retreating side (RS) in terms of average grain area for the AA2060 HAZ (Fig. 3). For the AA2099 HAZ, the RS exhibits a reduction in average grain area by 11 %, whereas the AS exhibits an increase in the average grain area by 24 % compared to the base metal of this alloy. It has been suggested that the coarsening (increase in size) of the grains in the HAZ AS of the AA2099 alloy is induced by the thermal effect during FSW [41]. Nevertheless, it is evident that the grain morphology of the HAZ region is similar to that of their parent alloy.

The distribution density of the intermetallic particles in the HAZ regions was found to be lower than the BM of their respective alloy (Fig. 4(a, b)). It is also observed that the coarse particles are much smaller within the HAZ regions, as seen in Fig. 5(a, b), especially for the AA2060 HAZ (approx. 40 % smaller than BM). These changes were also attributed to the FSW process, during which the heat generated helps in the dissolution of the precipitates. In contrast, the plastic deformation induced by the rotational movement of the tool changes the grain orientation and aids in the breakdown and redistribution of the coarse particles [1]. The dissolution of strengthening precipitates is also evidenced from the micro-hardness profiles of both alloys (Fig. 1c-d), where hardness reduction is observed towards the weld centre. The lowest microhardness that is observed in the HAZ-TMAZ interface of the AA2099 alloy is attributed to both the coarsening of grains in the HAZ region and dissolution of precipitates at the interface induced by the thermal effect of FSW [1,37,41].

The main differences in the microstructure between the HAZ AS and RS of either alloy are the differences in average grain area (Fig. 3), and the average size (Fig. 5) and distribution density (Fig. 4) of intermetallic particles, as discussed above, which were determined by detailed image analysis of the SEM micrographs. It has been found that these differences arise due to the asymmetry effects of FSW [55], during which the temperature distribution and relative speeds of plastic material on either side of the weldment are not the same [25,45,48].

The SZ of the AA2060 and AA2099 alloys (Fig. 2c and 2f) exhibit fine recrystallised grains, much smaller than the BM of their corresponding alloy. The reduction in average grain area for the AA2099 SZ is 62 %, whereas the reduction for the AA2060 SZ is a drastic 99.95 %, compared to the base metal of each alloy (Fig. 3). The coarse particles are very fine in this region and their distribution density is the lowest here, with a 67 % lower distribution for AA2060 SZ and 53 % lower distribution for AA2099 SZ compared to the intermetallic distribution density of their respective base metals (Fig. 4 and Fig. 5). This is due to the breakdown and redistribution of these particles during FSW [27]. It has been reported that the hardening precipitates in the SZ regions, such as T_1 in the AA2099 and T_1 and S' in the AA2060 alloys, are completely dissolved

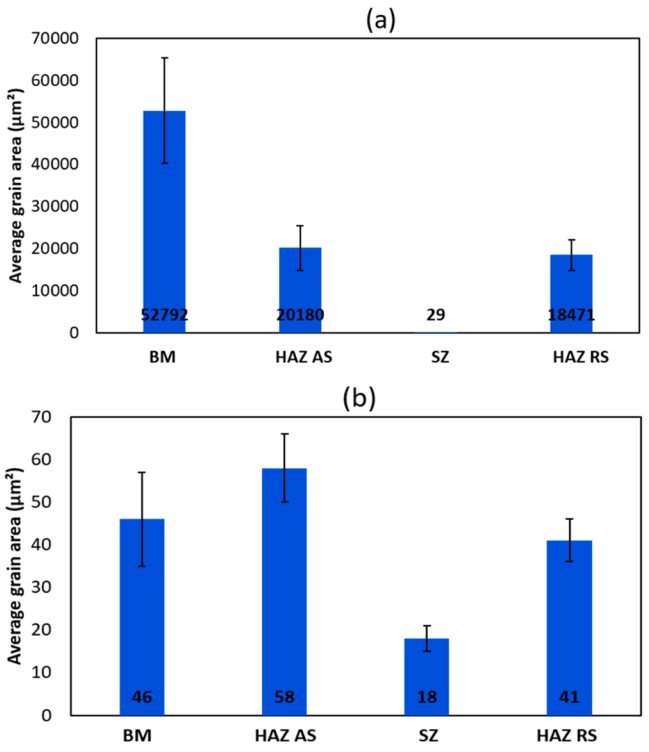

Fig. 3. Average grain area measured for the (a) AA2060 alloy weld zones, and the (b) AA2099 alloy weld zones.

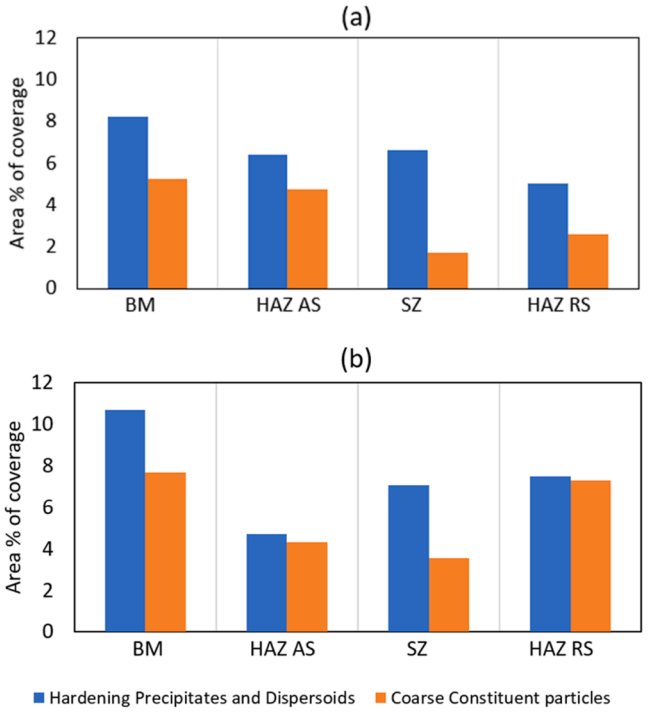

Fig. 4. Distribution density (population) of the intermetallic particles in the (a) AA2060 alloy weld zones, and (b) AA2099 alloy weld zones, given in terms of area percentage of total surface coverage.

due to the thermal influence during FSW [1,27,45]. This results in a severe drop in the micro-hardness of these regions, as seen in Fig. 1c and 1d, since the precipitates are the main strengthening phase particles in these alloys [16]. It has also been established by Donatus et al.[27] that

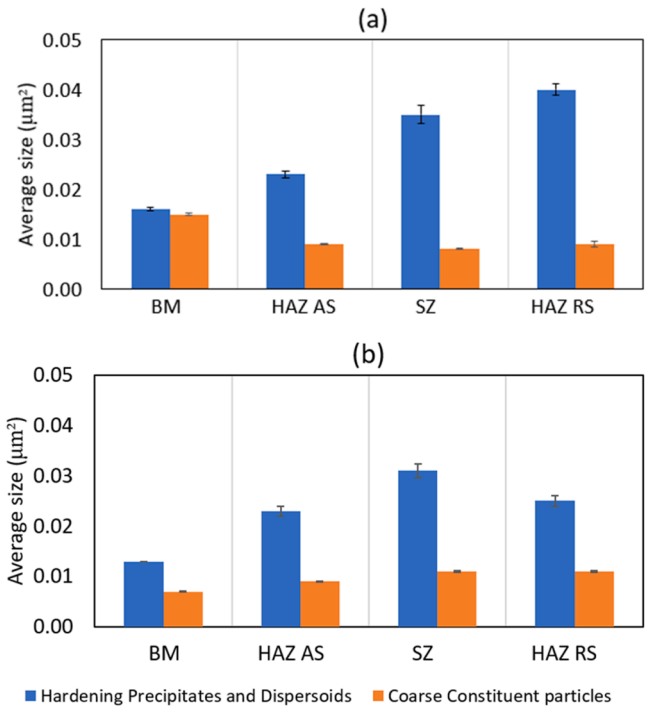

Fig. 5. Average size of the intermetallic particles found in the (a) AA2060 alloy weld zones, and (b) AA2099 alloy weld zones.

due to the dissolution of the hardening precipitates, the Li content in the solid solution of this region increases. However, this could not be confirmed since Li is undetectable by EDS analysis.

The dissolution of hardening precipitates in the SZ, as suggested by several researchers [1,27,45] and confirmed by the microhardness measurements, is not particularly evident from Fig. 4 (distribution density of intermetallic particles). This is due to the fact that during image analysis, both the dispersoids and the hardening precipitates are considered together as both are seen as dark particles in the SEM micrographs in Fig. 2. Therefore, even though there may be no hardening precipitates in the SZ, particles are still visible and quantified, indicating that dispersoids are still present in the region. Similar behaviour is also confirmed by the analysis in Fig. 5. As mentioned earlier, The dispersoids are larger than the hardening precipitates, resulting in a higher average size of the hardening precipitates and dispersoids within the HAZ and SZ regions compared to the BM. However, we do know that the BM has the highest concentration of dispersoids and hardening precipitates, the latter of which reduces the average size, as shown in Fig. 5.

The SZ of the AA2060 alloy, which corresponds to the weld nugget, exhibits an interesting microstructure due to the overlapping of alloys, as mentioned earlier. This overlapping within the SZ occurs due to the rotational movement of the tool pin during FSW, which causes stirring of the grains from both alloys [17]. Hence, the AA2060 SZ consists of layers of grains from the AA2060 alloy and the AA2099 alloy, as seen earlier in Fig. 1b. This feature of overlapping layers forming a banded structure was also observed by Bugarin et al. [22] in the dissimilar FSW of AA2024 and AA7475 alloys.

3.2. Electrochemical response and corrosion behaviour of the individual weld regions of the alloys

The electrochemical tests performed on the alloys give an insight into various details of the corrosion behaviour and quantify the corrosion kinetics of each weld zone. Additionally, in-situ time-lapse imaging during immersion tests was carried out to monitor the initiation and propagation of corrosion attack.

3.2.1. AA2060 alloy

The open circuit potential (OCP) of each weld zone for the AA2060 alloy as a function of time over 24 h in a 0.1 M NaCl solution is presented in Fig. 6. It is observed that the weld zones of AA2060 present relatively stable potentials throughout the experiment after the initial drop up to 4 h of immersion. The potential difference between the weld zones and the base metal is less than ± 50 mV, indicating that the heat and temperature due to the welding process do not have a major effect on the electrochemical nobility of the welded regions of this alloy. However, it is essential to note that the advancing and retreating sides of the HAZ regions exhibit the most different potential values, with the HAZ AS showing more noble potential than HAZ RS (approximately 100 mV), followed by the SZ and the BM. The difference in electrochemical response of the AS and RS of the HAZ is discussed later.

Fig. 4 shows the potentiodynamic polarisation curves of the welded regions BM (blue line), HAZ AS (orange line), HAZ RS (green line), and SZ (yellow line) of AA2060 alloy in a 0.1 M NaCl solution. The corrosion potential and corrosion current densities extrapolated from the curves are given in Table 2.

The BM and HAZ regions immediately undergo anodic dissolution upon anodic polarisation, indicated by the sharp increase in current density, showing negligible passivity. For the BM, between –528 to –414 mV vs Ag/AgCl, the increase in current density occurs at a slower rate. However, this is again followed by a rather steep increase in current density from –400 mV to –250 mV vs Ag/AgCl, indicating corrosion attack. The slower rate of increase in current density is likely due to the temporary blocking of anodic sites by the soluble corrosion products, which we also observe from the time-lapse in-situ immersion test images in Fig. 9 and the corresponding time-lapse videos given in SI.

The HAZ AS and RS regions show negligible differences in the polarisation curves and their corrosion potentials obtained by Tafel extrapolation. We do observe a small difference in the corrosion current densities between the two sides of the HAZ, as seen in Table 2. However, it is important to note that the differences in corrosion current densities of the HAZ AS and RS are within the standard error of margin. In the cathodic branch of the curves, we observe a diffusion-limited behaviour for the BM and HAZ regions, although this behaviour occurs for a slightly larger potential range for the BM.

The SZ region, similar to the BM and HAZ regions, exhibits immediate anodic dissolution upon anodic polarisation, as indicated by the drastic increase in current density seen in Fig. 7. The AA2060 SZ presents two distinct corrosion potentials in the potentiodynamic polarisation measurements, at –622 ± 8 mV and –837 ± 23 mV vs Ag/AgCl, respectively. The occurrence of this feature is discussed in detail later. The cathodic branch of the SZ too exhibits diffusion-limited behaviour, although the potential range where this occurs is much smaller here (from –912 to –1026 mV) compared to the BM and HAZ regions. From the polarisation curves, we observe only minor differences in the

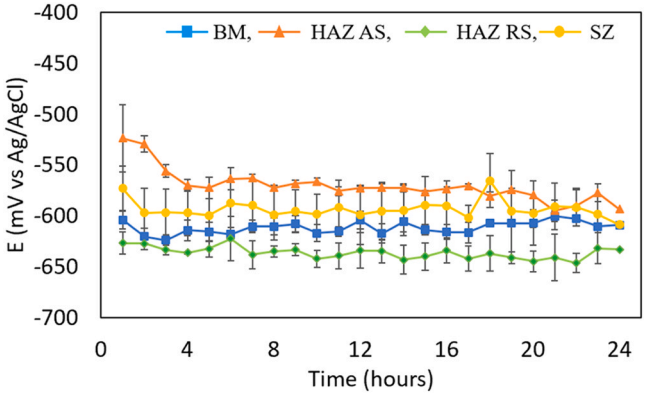

Fig. 6. OCP measurement of the AA2060 alloy weld zones over 24 h in a 0.1 M NaCl aqueous solution.

Table 2
Corrosion potentials and corrosion current densities for the AA2060 alloy weld zones obtained from the Tafel extrapolation of potentiodynamic polarisation curves displayed in Fig. 4.

Weld Zone	E_{corr} (mV vs Ag/AgCl)	i_{corr} (μA/cm^2)
BM	−588 ± 9	0.57 ± 0.35
HAZ AS	−572 ± 15	0.76 ± 0.31
HAZ RS	−570 ± 8	0.97 ± 0.47
SZ	−622 ± 8	0.22 ± 0.06
	−837 ± 23	7.25 ± 2.07

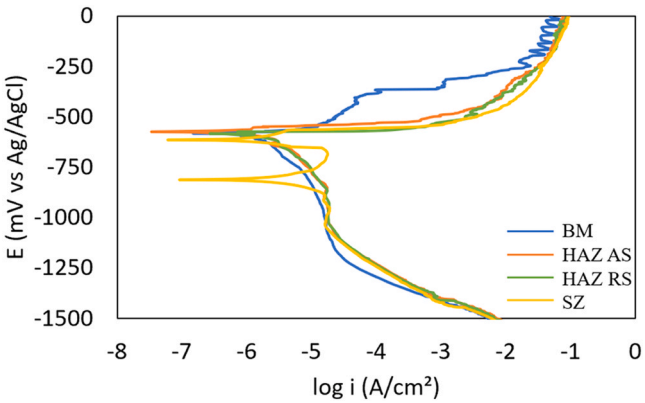

Fig. 7. Potentiodynamic polarisation curves of the AA2060 alloy weld zones in a 0.1 M NaCl aqueous solution. The anodic and cathodic polarisation curves were obtained separately.

corrosion activity between the weld regions. These differences occur mainly due to the welding process and the changes in microstructure induced by it. The difference in corrosion potential between the regions is within 50 – 60 mV, and all regions are dominated by localised attacks on anodic polarisation.

The linear polarisation resistance of the AA2060 weld zones monitored over 24 h is presented in Fig. 5. It is observed that among the zones, both the HAZ regions exhibit a higher resistance, followed by the SZ, whereas the BM exhibits the lowest polarisation resistance throughout the experiment. The initial resistance values are within the range of 5 – 12 kΩ.cm^2. After the initial decrease in resistance (Fig. 5), an increase in resistance is observed for all the weld regions at 4 – 5 h of immersion. However, within a couple of hours, the resistance of the weld zones decreases again. This phenomenon is repeated at 10 – 15 h of immersion for the HAZ regions of this alloy. The SZ region of the AA2060 alloy exhibits the least fluctuations in resistance throughout the experiment, indicating a more uniform corrosion attack.

The optical micrographs for the AA2060 BM, HAZ RS, and SZ, obtained before immersion, at 1 h, and 3 h during the in-situ time-lapse immersion tests in 0.1 M NaCl solution are shown in Fig. 6. The corresponding time-lapse videos of the experiment over 24 h is given in the Supplementary Information (SI). Since the attack morphology for HAZ in AS and RS were similar, only the micrographs for the HAZ RS are shown here. The attack on the AA2060 alloy weld zones was observed to initiate within the first 10 – 15 min of immersion with the formation of a corrosion ring. The formation of corrosion rings has been found to occur due to counter ionic flow of metal ions originating from the anode and hydroxide ions developed at the cathode [38]. These metal ions and hydroxide ions meet at a distance away from the anode, thus forming a ring of corrosion products as seen in the Fig. 9. At the centre of the corrosion ring, a dark spot is observed from where gas bubbles evolved, as seen in the micrographs obtained after 1 h of immersion in Fig. 9. This dark region is identified as the attack site, and the gas bubbles suggest anodic H_2 gas evolution. This was also reported in the work of Donatus et al. [23] on the AA2198 alloy welded by FSW.

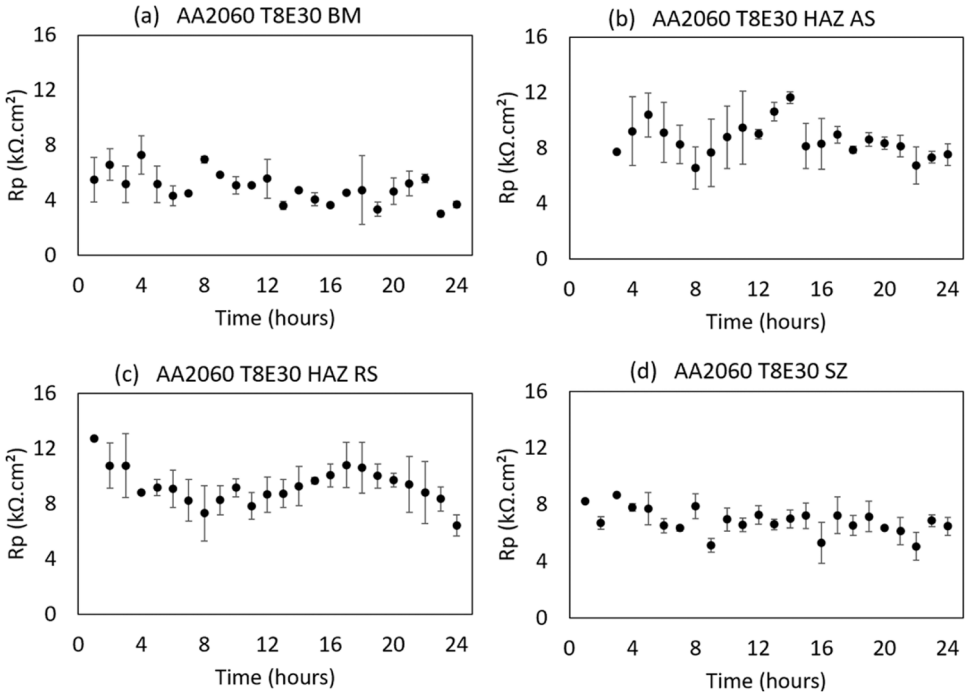

Fig. 8. LPR measurement of the AA2060 alloy weld zones as a function of time over 24 h in a 0.1 M NaCl aqueous solution.

After 1 h of immersion for the BM and HAZ regions, darkening at the sites of coarse particles is observed with increasing immersion time, suggesting an attack around these particles. These sites grow in size as the experiment progresses, as seen from the AA2060 BM and AA2060 HAZ RS time-lapse videos in SI. Outside the corrosion ring, a relatively uniform attack on the entire surface is seen, corroding the topmost layers of grains in this alloy.

For the AA2060 SZ (Fig. 9c), the region outside the corrosion ring presents a slightly complex corrosion behaviour. In the first image, at 0 h of immersion, we observe the overlapping layers of the two alloys in the AA2060 SZ, as discussed earlier. These layers have been marked with black lines to show the overlapping. After 1 h of immersion, a preferential attack is observed in specific layers, indicated by the darkening of these layers in Fig. 9c (1 h). The remaining layers in the SZ undergo attack only after 2 – 3 h of immersion, and are labelled as the non-preferentially attacked layers. This preferential attack is clearly seen in the AA2060 SZ time-lapse video in provided in the SI.

After a few hours of immersion, the surface of the weld zones was completely covered with corrosion products, limiting us from further analysis by in-situ time lapse immersion tests. To study the full effect of the immersion tests, the samples were removed after 24 h of immersion and desmutted for 15 seconds in a 30 % HNO_3 solution to remove the oxide products. They were then studied under SEM and the exposed areas of the immersion test are shown in Fig. 7.

In the BM, two corrosion rings are observed, as seen in Fig. 7a. Multiple attack sites joined by intergranular corrosion are observed within the corrosion rings (Fig. 10b). These attack sites have been referred to as severe localised corrosion (SLC) in other works [3,23,54]. An EDS scan around these sites revealed that these regions were rich in Cu content. The exposed area of the AA2060 BM outside the corrosion ring presented a relatively uniform surface. During the immersion test (Fig. 6a), it was observed that this region is also attacked. However, it is a gradual process that lasts for several hours (as seen by the AA2060 BM time-lapse video in SI). This attack starts in selected grains and is later propagated to the other grains on the surface. This is referred to as the selective dissolution of the strain-deformed grains on this alloy [47]. Once all the grains are attacked, a thick build-up of corrosion products is found on the surface. When the corrosion products are removed from the surface by de-smutting, an entire layer of corroded grains is removed, thus showing a relatively uniform surface. However, from Fig. 10a, we do observe a small region where an extra layer of grains is dissolved, thus demonstrating the effect of selective dissolution of grains. During this process, the smaller pits are also removed from the surface.

At the edges of the region exposed to the electrolyte, Cu rich particles were observed by EDS analysis (Fig. 7a). These particles are likely formed due to redeposition of Cu from the dissolution of coarse constituent particles of this alloy. This has also been observed in the work of Zhu et al. on the AA2060 alloy [12], and is discussed later.

The HAZ region (Fig. 7c) presented corrosion behaviour similar to the BM of the alloy. Additionally, the attack site presented a significant intergranular attack ranging in size from 130 to 250 μm in length, as seen in Fig. 7d. Unlike the BM, both HAZ and SZ regions exhibit a protected region inside the corrosion ring. It is proposed that since the attack sites act as the anode, the remaining region within the corrosion ring acts as the cathode, thus protecting itself from corrosive attack [23]. However, this phenomenon was not observed in the corrosion ring of the BM, most likely due to the higher concentration of the active hardening precipitates, as seen in Fig. 4(a).

The SZ of the AA2060 alloy presented a more complex corrosion behaviour (Fig. 7e). This is attributed to the difference in alloying elements found in different regions of the SZ. In this region, i.e. the weld nugget, layers of grains from the AA2099 and AA2060 alloys overlap due to the FSW process. Due to this, the AA2099 alloy layers exhibit immense pitting, whereas the layers from the AA2060 alloy present a uniform surface due to the dissolution of entire grains, as observed for the BM and HAZ of the AA2060 alloy. The layers corresponding to the preferential attack in Fig. 9c originate from the AA2060 alloy, while the non-preferentially attack layers were from the AA2099 alloy. This feature is visible in Fig. 10e, with the different layers exhibiting different attack mechanisms. This attack mechanism is also revealed from the AA2060 SZ time-lapse video in SI. This dual attack could possibly be the reason why two distinct corrosion potentials are observed for the AA2060 SZ in potentiodynamic polarisation measurements in Fig. 7 and Table 2.

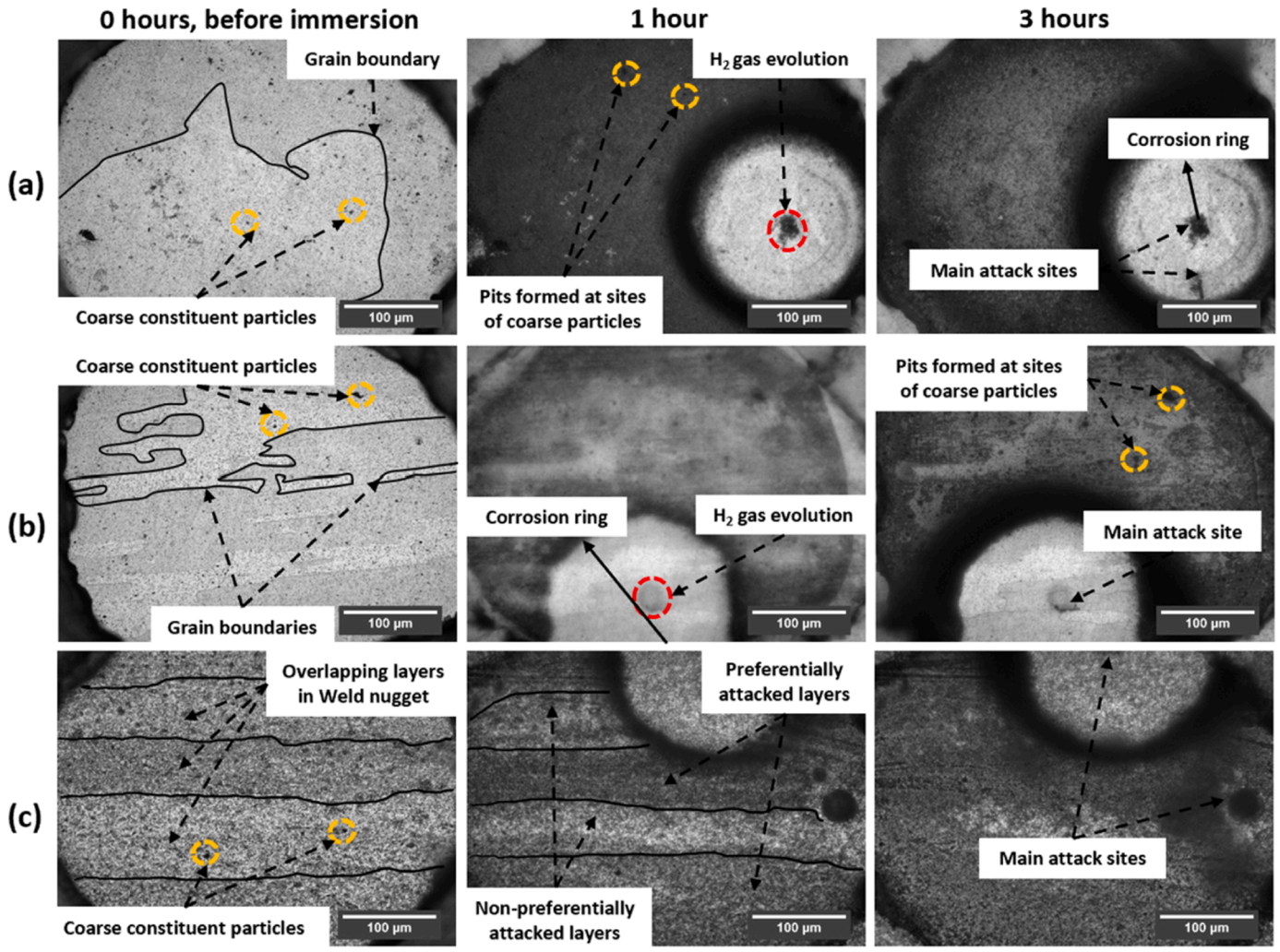

Fig. 9. Optical micrographs of in-situ time-lapse immersion test of the weld zones of AA2060 alloy in a 0.1 M NaCl aqueous solution at 0 h (before immersion), 1 h, and 3 h: (a) BM, (b) HAZ RS, and (c) SZ.

3.2.2. AA2099 alloy

The OCP of the AA2099 weld zones in a 0.1 M NaCl solution over 24 h is presented in Fig. 11. The different weld zones experience considerable potential fluctuations throughout the experiment time of 24 h. An initial drop in potential is observed within the first three hours of immersion for all the weld zones. The BM of this alloy becomes the most active after 1 h of immersion. This sudden drop of potential is likely due to the high concentration of the active hardening precipitates found in this region, as seen in Fig. 4(b), which are attacked within the first hour of immersion. The drop in OCP after 1 h is not as severe for the other zones of the alloy.

Unlike the other weld regions, the HAZ AS experiences more variations in its potential between 3 – 8 h of immersion. After 8 h of immersion, the AA2099 weld zones still do not exhibit stable potentials like those observed for the AA2060 weld zones. Instead, we observe slight fluctuations in potential values for all the weld regions of this alloy until the end of the experiment, thus indicating higher reactivity of the AA2099 alloy. Similar to the AA2060 HAZ regions, the AA2099 HAZ AS and RS exhibit different electrochemical activity from each other with potential differences ranging from a meagre 25 mV to a drastic 100 mV between them at the same experimental time. Further discussion on this phenomenon is provided in the following sections.

The potentiodynamic polarisation curves of the AA2099 weld zones obtained in a 0.1 M NaCl solution are shown in Fig. 12. The corrosion potentials and corrosion current densities determined from Tafel extrapolation are given in Table 3. It is observed that the polarisation curves of the AA2099 alloy weld zones – anodic and cathodic branches, are quite similar to each other. The BM (blue line) and HAZ regions (orange line for AS, green line for RS) show anodic dissolution immediately on anodic polarisation. The difference in corrosion potentials between the regions is less than 15 mV. No distinguishable passive domain is observed for these regions. The SZ region (yellow line), however, does exhibit a distinct pitting potential in its anodic branch at –548 mV vs Ag/AgCl, similar to the AA2060 SZ. The cathodic branches of the polarisation curves exhibit diffusion-limited behaviour for all weld zones.

The linear polarisation resistance of the AA2099 weld zones monitored over 24 h are shown in Fig. 10. The trend of corrosion resistance observed for the AA2099 weld regions is also to decay with time; however, for the BM, there is an increase towards the end of the experiment. The initial resistance of the zones is within the range of 10 – 14 kΩ.cm^2, much higher than that of the AA2060 alloy weld zones. It is observed that both the HAZ regions of this alloy have higher resistance than the BM and the SZ. The SZ presents the least resistance amongst all the zones and has a larger but steady decay over the 24 h of immersion.

The BM initially exhibits a high resistance, but it decreases significantly once the experiment starts until 7 h of the experiment. An increase for the next 5 h is observed, suggesting that attack is restricted in this domain. This decrease and increase in resistance trend was observed again between 12 – 24 h, also seen from the OCP measurements in

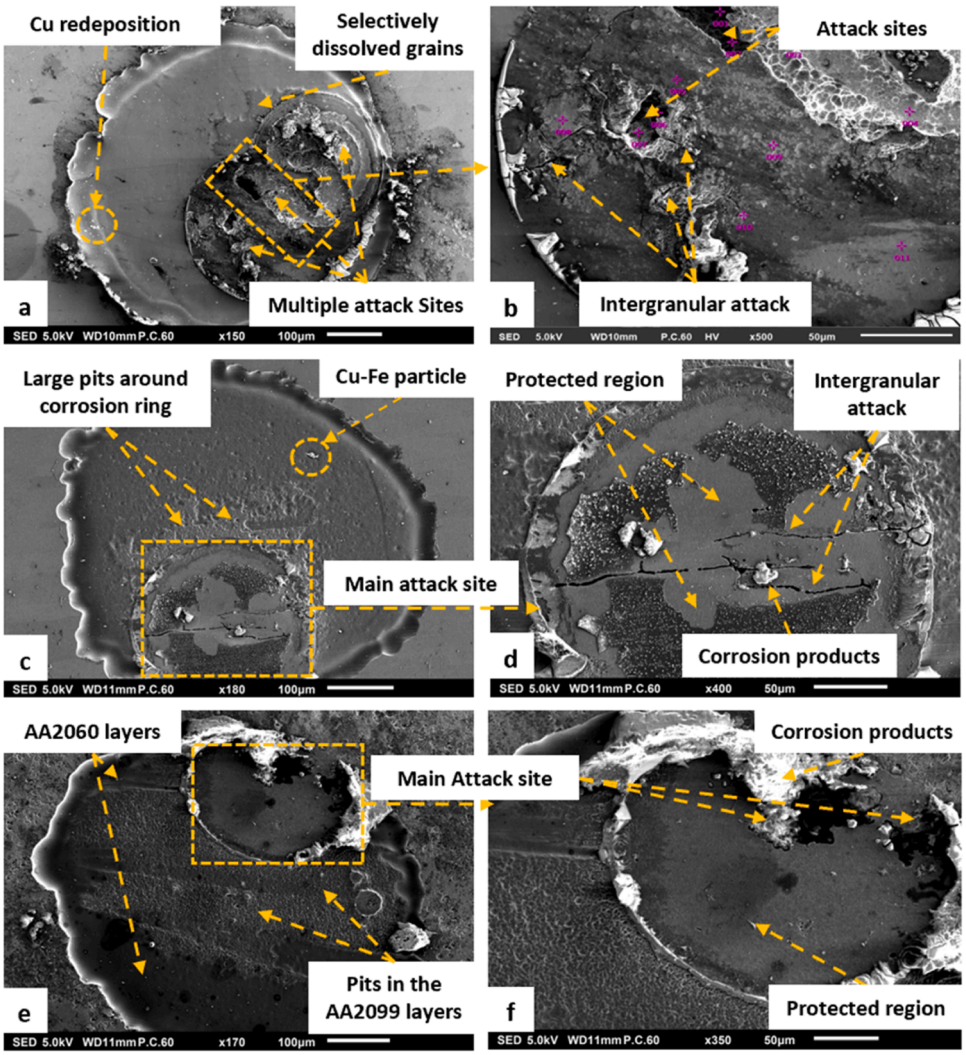

Fig. 10. SEM images of exposed area of in-situ immersion test of the AA2060 weld zones after 24 h of immersion and de-smutting in 30 % HNO_3 solution: (a, b) BM, (c, d) HAZ RS, and (e, f) SZ.

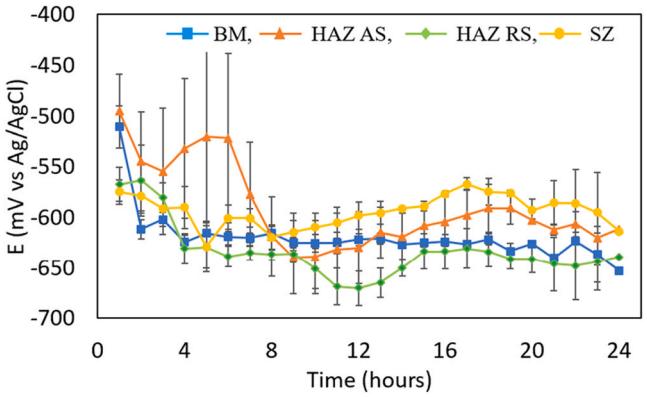

Fig. 11. OCP measurement of the AA20099 alloy weld zones over 24 h in a 0.1 M NaCl aqueous solution.

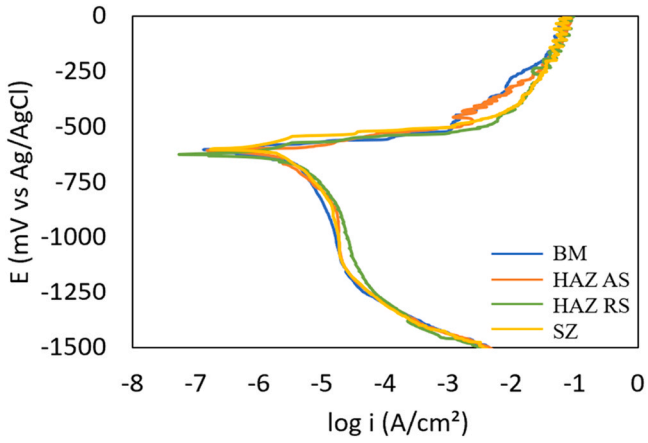

Fig. 12. Potentiodynamic polarisation curves of the AA2099 alloy weld zones in a 0.1 M NaCl aqueous solution. The anodic and cathodic polarisation curves were obtained separately.

Fig. 11. The HAZ regions exhibit this increase after 4 – 5 h of immersion and present rather high resistance at 7 – 8 h of immersion, after which there is a gradual decrease in resistance till the end of the experiment at 24 h. It is proposed that this resistance increase is most likely due to the formation of corrosion products, which can deposit on the surface and temporarily restrict further surface attack. However, these corrosion products are not entirely stable or well attached to the surface. Therefore, attack is resumed once these products are detached or removed from the surface.

Table 3
Corrosion potentials and corrosion current densities for the AA2099 alloy weld zones obtained from the Tafel extrapolation of potentiodynamic polarisation curves displayed in Fig. 9.

Weld Zone	E_{corr} (mV vs Ag/AgCl)	i_{corr} (μA/cm^2)
BM	−602 ± 2	0.38 ± 0.12
HAZ AS	−607 ± 3	0.21 ± 0.06
HAZ RS	−615 ± 13	0.12 ± 0.01
SZ	−640 ± 23	0.20 ± 0.05

The optical micrographs of the AA2099 weld zones obtained before immersion, at 1 h, and 3 h during the in-situ time-lapse immersion tests over 24 h are shown in Fig. 11, and the corresponding time-lapse videos of the experiment over 24 h are found in the Supplementary Information (SI). The corrosion attack in the BM and HAZ starts immediately as the chloride ions from the electrolyte come in contact with the surface, forming corrosion rings within the first 10 min, indicating the highly active behaviour of this alloy. This was followed by H_2 gas evolution from the centre of the corrosion rings, shown in the micrographs in Fig. 11, which were later identified as the primary attack sites that grow in size with increasing immersion time, forming SLC sites. Additionally, darkening of the grain boundaries was observed after 1 h of immersion from the AA2099 BM and AA2099 HAZ RS time-lapse videos in SI, indicating attack in these regions. Similar to the AA2060 alloy in-situ time-lapse immersion tests, darkening at the sites of coarse constituent particles was observed, indicating attack on these particles with increasing immersion time.

For the SZ of the AA2099 alloy, the corrosion ring formed an hour after immersion, indicating a slower attack in this region, as seen by the AA2099 SZ time-lapse video in SI. The attack on the SZ is dominated by pitting corrosion on the surface which starts within the first hour of immersion, as seen in Fig. 11c. Over time, it is observed that pits are formed on the entire surface outside the corrosion ring. However, after 2 – 3 h of immersion, only the larger pits exhibit lateral propagation, as is evident from Fig. 11c at 3 h of immersion. Similar to the AA2060 alloy, the surface is entirely covered with corrosion products after 4 h of corrosion, thus limiting our analysis with this method.

Fig. 12 shows the SEM images of the weld zones after 24 h of the immersion test followed by de-smutting as described earlier. The BM and the HAZ regions of the AA2099 alloy exhibit severe intergranular attack, as seen in Fig. 12a and 12c. This attack is observed to be more prominent in this alloy than in the AA2060 alloy regions, even though both alloys contain the hardening T_1 precipitate, as reported in the literature [1,42,46,49]. This effect is due to the smaller size of the grains of the AA2099 alloy, where these strengthening particles nucleate on grain boundaries, unlike the AA2060 alloy, where the grains are large and the strengthening particles are more homogeneously spread throughout the surface, leading to a higher distribution density of these particles in the AA2099 alloy (approximately 30 % higher) compared to the AA2060 alloy, as seen in Fig. 4.

Additionally, trenches formed around some of the coarse constituent particles indicating that these Cu-rich coarse particles are more noble than the alloy matrix, thus causing them to act as cathodes and the alloy as the anode. This leads to the dissolution of the alloy matrix around the coarse particles, as seen in the enlarged inset in Fig. 15a. This phenomenon was also reported by Ma et al. [54] in their study of the AA2099 alloy localised corrosion behaviour. In some cases, the alloy matrix around a particle is attacked to such an extent that the coarse particles detach from the surface. This leaves large pits/cavities on the surface of the matrix, as observed in Fig. 12a and 12c.

Since the hardening precipitates are not found in the SZ, intergranular attack is not observed in the region. Instead, the SZ is covered with pits on the entire surface, as seen in Fig. 12e. This is attributed to two factors – the high Li content in the solid solution of the SZ due to the dissolution of the hardening precipitates and the presence of fragmented Cu-rich coarse constituent particles, which are distributed evenly on the surface and are less active than the hardening precipitates [23]. This causes a more uniform attack in the SZ region than in the BM or the HAZ regions, as seen in the immersion test (Fig. 11c) and the LPR measurements (Fig. 10d).

3.3. Corrosion performance of the entire welded region of the alloys

The corrosion behaviour and galvanic interaction between the weld zones of the AA2060 and AA2099 alloys were studied by performing surface potential measurements in a chloride environment using the

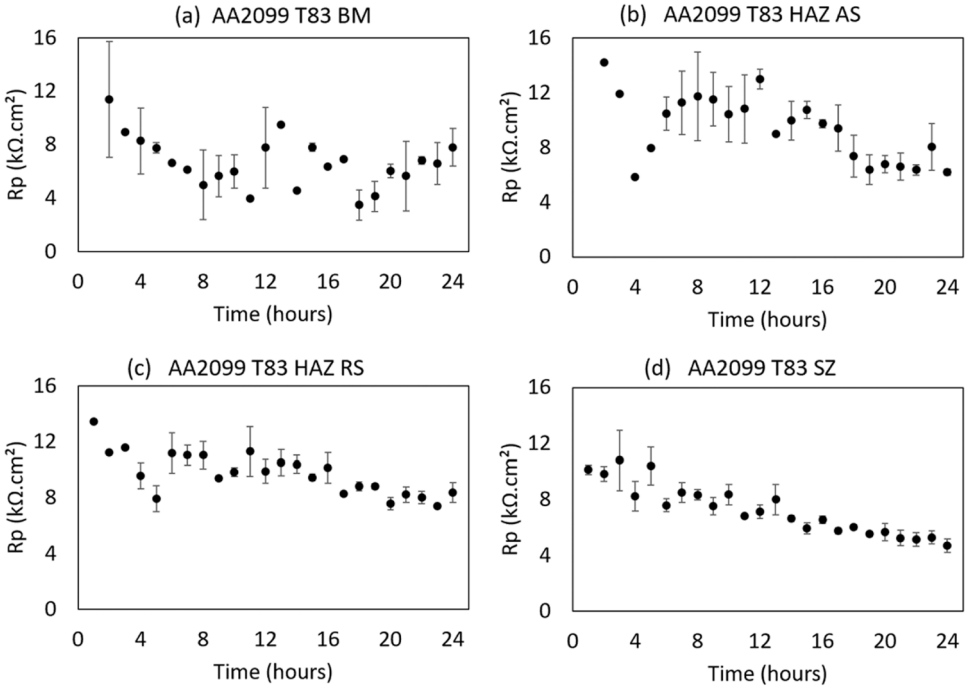

Fig. 13. LPR measurement of the AA2099 alloy weld zones over 24 h in a 0.1 M NaCl aqueous solution.

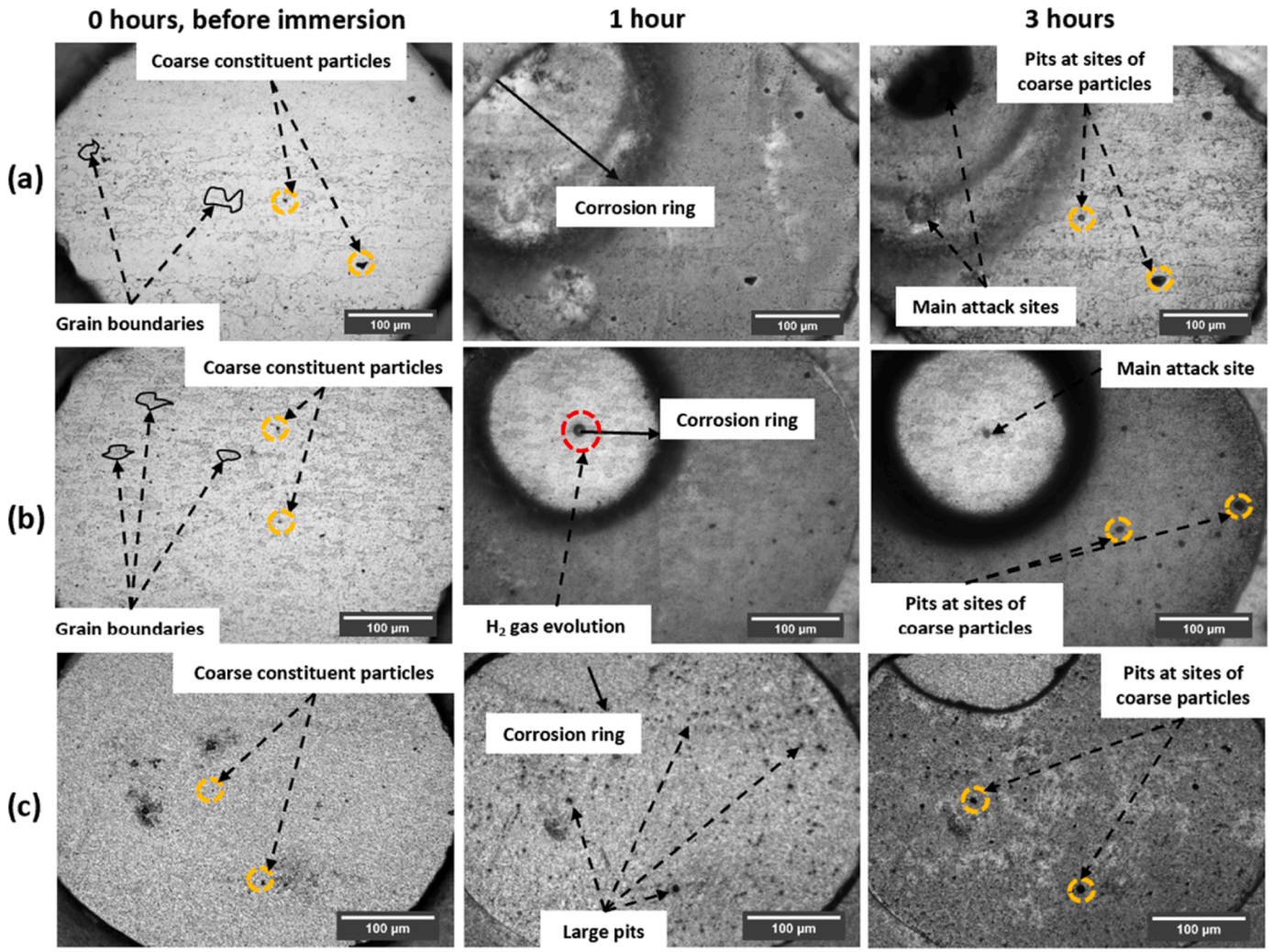

Fig. 14. Optical micrographs of in-situ time-lapse immersion test of the weld zones of AA2099 alloy in a 0.1 M NaCl aqueous solution at 0 h (before immersion), 1 h, and 3 hs: (a) BM, (b) HAZ RS, and (c) SZ.

scanning Kelvin probe (SKP), and in-situ time-lapse immersion test for the entire weld joint. The SKP tests under ambient, high humidity, and chloride environment conditions highlight the anodic and cathodic activity regions in the dissimilar weld zones. The immersion test on the weld joint presents the initiation and propagation of the corrosion attack over time.

The surface potential of the entire weld region was measured under a thin film of evaporated 0.1 M NaCl solution to induce a corrosive environment. The region scanned under SKP is seen in Fig. 16a, and the subsequent surface potential maps obtained at different exposure times are shown in Fig. 16b – 13f. The lowest potentials correspond to areas of anodic activity, whereas the less negative potentials are cathodic regions on the surface. The approximate weld regions have been marked in the SKP surface potential maps to better aid in the interpretation of the results.

It is observed that after 1 h, the region within the AA2060 SZ exhibits highly anodic behaviour compared to the AA2099 side (Fig. 16b). The surface potential distribution is not uniform even within the alloy, thus showing very localised anodic sites. The HAZ regions of the AA2060 alloy and the SZ of the AA2099 also exhibit relatively high anodic activity. Meanwhile, the HAZ regions of the AA2099 alloy and the BM of both alloys are the cathodic regions during this point of time. After 2 h (Fig. 16c), the surface potentials in the weld zones of each alloy become relatively uniform over time. The AA2060 alloy presents a lower surface potential compared to that of the AA2099 alloy, indicating that it is the anodic region whereas the AA2099 alloy is the cathodic region. This is in agreement with the results obtained from OCP monitoring (Fig. 6 and Fig. 11) and LPR measurements (Fig. 8 and Fig. 13), where we observe more noble potentials for the AA2099 alloy weld zones and also higher polarisation resistivity compared to those for the AA2060 alloy weld zones.

The surface potential of the AA2099 alloy weld zones drops considerably after 3 h, making this alloy the anodic region instead of AA2060. This is in agreement with the LPR measurements of the AA2099 alloy weld regions (Fig. 10) where a drop in resistance after 3 h of immersion is observed. In the HAZ of the AA2099 alloy, small regions exhibit a more pronounced negative surface potential than the remaining surface. Although this effect is already seen in a few regions after 2 h, its visibility is amplified after 3 h of exposure to the chloride environment. These regions are associated with sites of intermetallic coarse constituent particles that are initially anodic in nature due to the presence of active elements such as lithium, magnesium, manganese, and iron.

The next scan, performed after 4 h, is shown in Fig. 16e. It is observed that the AA2099 alloy has a much higher surface potential than the previous scan, with a potential increase from –1100 mV to –400 mV, indicating much lower activity in this region. However, the HAZ RS and the SZ of this alloy do exhibit anodic activity compared to the rest of the alloy. We also observe a considerable increase in potential at the sites of the intermetallic particles in the AA2099 HAZ regions from its highly

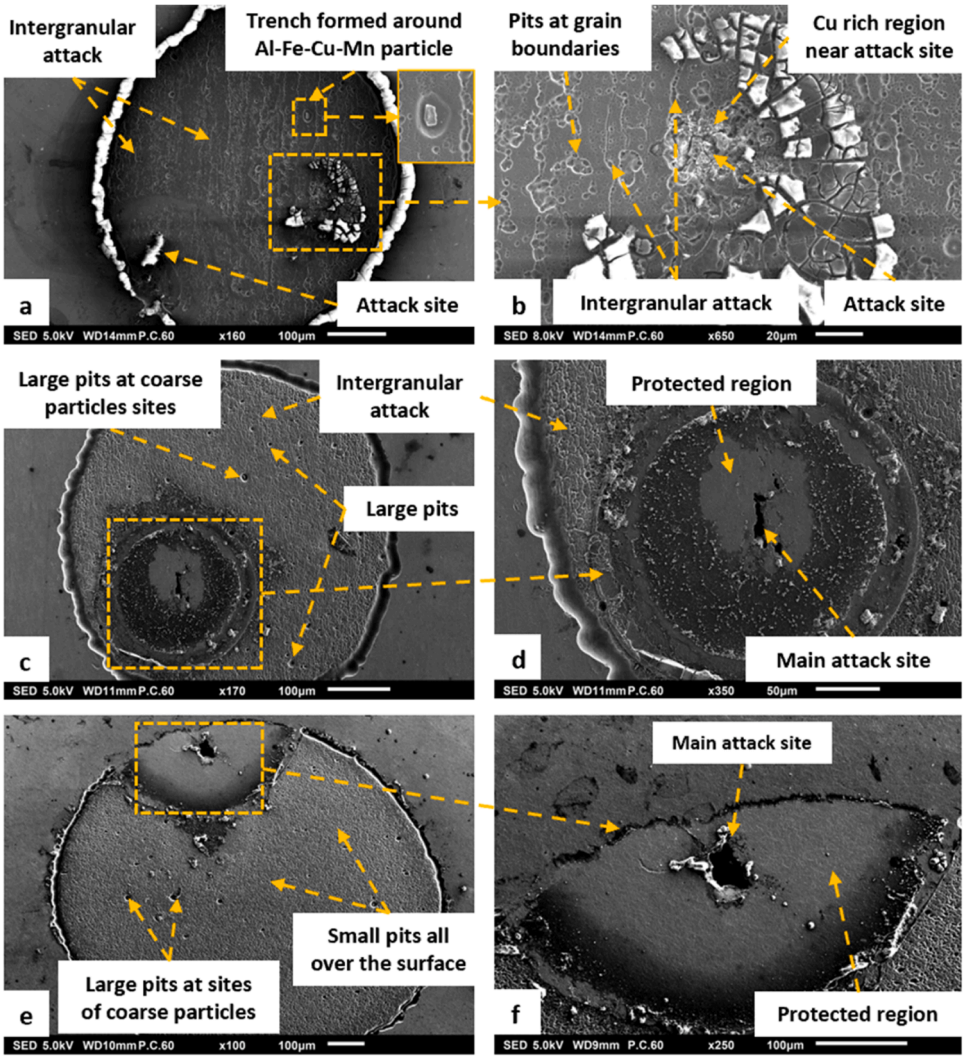

Fig. 15. SEM images of exposed area of in-situ immersion test of the AA2099 weld zones after 24 h of immersion and de-smutting in 30 % HNO_3 solution: (a, b) BM, (c, d) HAZ RS, and (e, f) SZ.

negative potentials seen after 3 h. This increase occurs due to the dissolution of the active elements in the intermetallic particles, thus leaving behind more noble elements, such as copper, which are then cathodic with respect to the aluminium matrix [54,56]. Regarding the AA2060 alloy, highly localised activity is observed in the retreating side of the AA2060 SZ, whereas the remaining regions of the AA2060 alloy exhibit relatively stable surface potentials. This is in line with the OCP monitoring of the AA2060 weld zones (Fig. 6), where we observe relatively stable potentials after 4 h of immersion.

The last scan, Fig. 16f, was performed after 5 h under identical experimental conditions. The regions under anodic influence in the previous scan decreased considerably with the surface potential of the AA2060 weld regions approaching that of the AA2099 alloy. The highest region of anodic activity observed is still within the SZ of the AA2060 alloy.

The in-situ images for the weld joint of both alloys immersed in 0.1 M NaCl solution at various time intervals are shown in Fig. 14 and the weld joint time-lapse video given in SI. It is observed that an attack has initiated in the AA2060 SZ within the first hour of immersion (Fig. 14a). However, the attack does not occur in the entire region of the SZ of this alloy. The retreating side of the SZ exhibits more darkening, indicating a larger attack. This is similar to the localisation of the attack at the AA2060 SZ observed by the SKP measurements after 1 h of exposure to the chloride environment in Fig. 16b.

Over the next hour of immersion, Fig. 14b, the AA2099 SZ starts darkening due to attack within this region. The BM and HAZ regions of the AA2060 alloy also start to corrode during this time. This is in agreement with the SKP measurements (Fig. 13b), where high anodic activity was observed in these regions compared to the AA2099 BM and HAZ, which were more cathodic in nature.

After 3 h of immersion, the HAZ regions of the AA2099 alloy remain protected and still present a mirror surface finish. On the other hand, the BM of this alloy exhibits a few attack sites with protected regions surrounding them, suggesting the formation of SLC sites as observed during the in-situ immersion test of the weld zone in Fig. 11a. Although this was also observed in the BM of the AA2060 alloy, it was limited to a few sites.

As the immersion test progresses for the next couple of hours, in Figs. 17d and 14e, the AA2060 alloy weld zones are continuously attacked, resulting in a visually even surface due to the formation of oxide products. During this time, the advancing side of the AA2060 SZ is attacked, as shown by the SKP measurement after 4 h in Fig. 16e. On the AA2099 alloy, attack initiation and propagation are observed in the HAZ regions (AS and RS) after 4 h of immersion (Fig. 17d). This observation is in good correlation with the SKP results obtained after 4 h of exposure to the chloride environment (Fig. 16e). This correlation also confirms the cathodic activity of the remaining zones of the AA2099 alloy at 4 – 5 h of exposure, which undergo attack on increased exposure time, as seen in Fig. 14f (6 h of immersion).

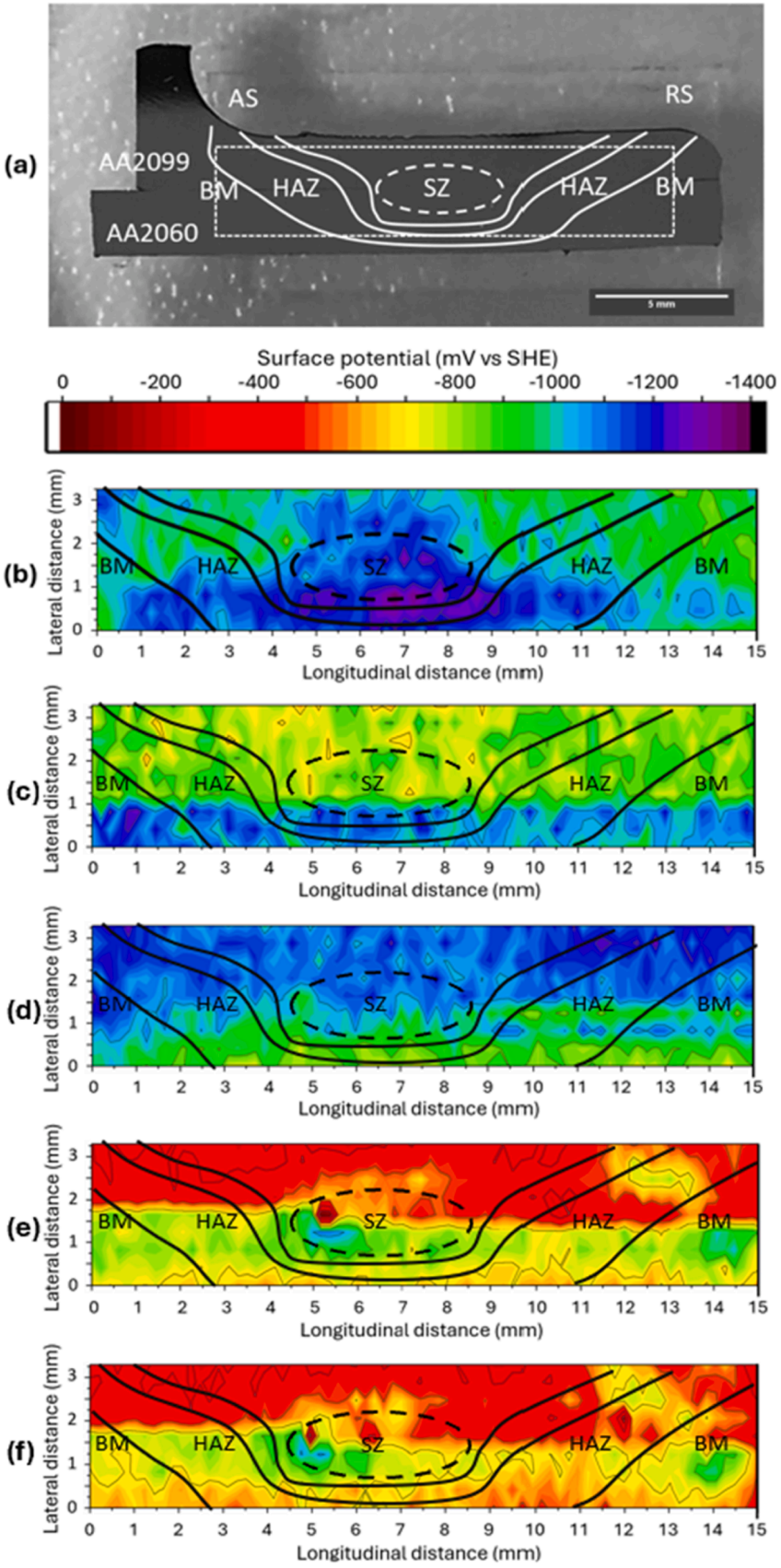

Fig. 16. SKP surface potential maps obtained for the weld joint of the AA2099 and AA2060 alloys under a thin film of evaporated 0.1 M NaCl solution, rehydrated at 93 % RH and T of 21.6°C (a) Region of weld joint scanned under SKP after (b) 1 h, (c) 2 h, (d) 3 h, (e) 4 h, and (f) 5 h. The approximate weld regions are marked in the surface potential maps according to the distance from the start point.

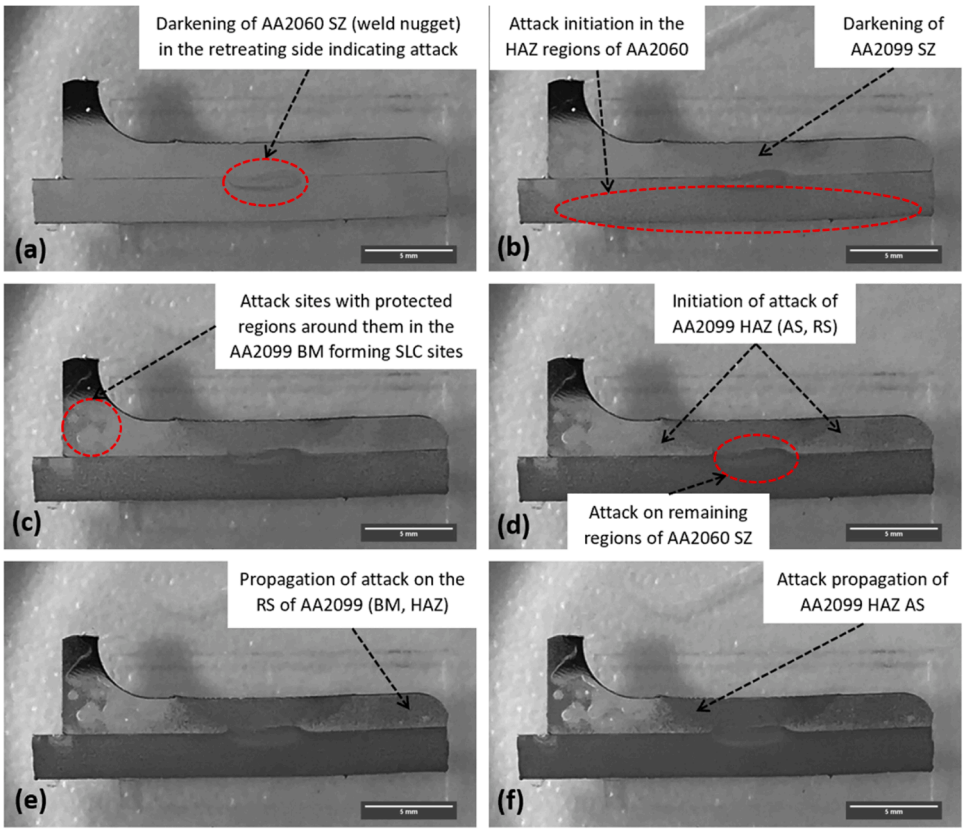

Fig. 17. In-situ time-lapse immersion test of the AA2099 and AA2060 FSW joint in 0.1 M NaCl solution at: (a) 1 h immersion, (b) 2 h immersion, (c) 3 h immersion, (d) 4 h immersion, (e) 5 h immersion, and (f) 6 h immersion.

3.4. Discussion

The welding of dissimilar aluminium-lithium alloys is bound to have an intricate effect on the microstructure and, eventually, the electrochemical behaviour of the weld joint. It is observed that the structure of both sides of the weld joint is different from each other in terms of shape and size (Fig. 1). Evidence in the literature suggests that during the FSW process, there is a difference in the relative speeds of plastic material in the advancing side (AS) and retreating side (RS), caused by the irregular heat distribution in each side [25]. This results in a higher temperature distribution in the AS of the HAZ, thus giving a sharper profile and a larger width of this region, compared to the smaller RS of the HAZ, which experiences lower temperatures during FSW [45], as seen by the Vickers Microhardness measurements along the weld profile.

The AA2099 alloy was identified as the more active alloy based on the lower corrosion potentials obtained during potentiodynamic polarisation and the lower OCP values over 24 h. This is due to the higher lithium content in this alloy, as seen in Table 1. However, the difference in potential between the two alloys during OCP measurements is within 20 mV, thus indicating that the reactivity of the two alloys is comparable. Meanwhile, the AA2060 weld zones exhibited considerable stability of the OCP values (Fig. 6) compared to the AA2099 weld zones over 24 h. This relative stability has been attributed to the cold rolling of the AA2060 alloy during the production process, which allows for a more homogeneous distribution of the active hardening precipitates such as the T_1 particles [8], thus reducing the drastic fluctuations in potential values, unlike that seen for the AA2099 alloy weld zones in Fig. 11.

The SZ regions of both alloys exhibit similar potential values over 24 h. This is possibly due to the mixing of alloying elements of both alloys in the SZ regions. We also observed that the attack in these SZ regions is more gradual compared to the BM and the HAZ regions, as seen by the LPR measurements, which is mainly attributed to the dissolution of the highly active lithium-containing T_1 precipitates in this zone during FSW [1,23,27]. However, the dissolution of these particles leads to a higher Li content in the solid solution of the SZ [27], which is why the linear polarisation resistance values of the SZ regions are the lowest amongst the weld zones. The HAZ regions presented higher polarisation resistance than the BM of their corresponding alloy. It is suggested that this was due to the sparse distribution of the hardening precipitates in the HAZ regions compared to the BM, as evidenced by the distribution density of these particles (22 % – 56 % lower) in Fig. 4 and by the microhardness in Fig. 1(c and d). The HAZ regions also exhibited a higher resistance than the SZ, where the precipitates are completely dissolved but a higher Li content in solid solution is present.

Although the attack mechanism is similar for the HAZ AS and RS regions, their electrochemical activity is inconsistent within the same alloy, as seen by the OCP measurements in Fig. 6 and Fig. 11. It is suggested that this is due to the differences in the distribution density of intermetallic particles, the average size of these intermetallic particles, and the grain size in these regions. These changes occur due to the irregular heat distribution and the difference in relative speeds of plastic material on both sides during FSW [25,45,48], as mentioned earlier. It has been determined that the average grain area of the AS is comparatively larger than that of the RS. This plays an important role here since it results in more nucleation sites at the grain boundaries for the hardening precipitates in the RS. It has also been found that the average size of the coarse constituent particles in the RS is larger compared to the AS in both alloys. These factors cause the RS to be ever so slightly more active as compared to the AS of the alloy, also indicated by their lower OCP values in Figs. 4 and 9 and their lower polarisation resistance values in Figs. 5 and 10.

The formation of SLC sites during immersion tests has been attributed to the dissolution mainly of the hardening precipitates (T_1) at

cluster sites [28,53]. Since the T_1 (Al_2CuLi) precipitate is highly active, it acts as an anode with respect to the matrix, during which the lithium dissolves over time and copper enriches on its surface layer [16,57]. The corroded particle then becomes cathodic to the substrate, leading to the anodic dissolution of the matrix around it. This has been referred to as the selective dissolution of the T_1 precipitates by others [54,58]. During this process, corrosion products deposit near the mouth of the pits which causes acidification within the pits, leading to a greater degree of attack in these regions and forming SLC sites [3]. The selective dissolution of the T_1 precipitates is also why Cu-rich areas are observed in the proximity of attack sites from EDS analysis of the SEM images presented in Fig. 10 and Fig. 15.

Similarly, the S′ phase particles in the AA2060 alloy are highly active compared to the alloy matrix due to their magnesium content [12], thus acting as local anodic sites that induce corrosion attacks. Wint. et al. [59], in their work on AA2024 alloy, proposed that since the particle is more active than the matrix, it is galvanically attacked until all the Mg^{2+} and Al^{3+} ions are released from the particle. The remainder is a porous Cu sponge which, along with the Cu^{2+} ions, are then redistributed and replated on the surface of the alloy, leaving pits or cavities at these sites. This redeposition of copper is observed from the SEM images of the alloy, especially towards the edges of the exposed area, as seen in Fig. 7a.

The timeline of corrosion attack in the weld zones from the in-situ time-lapse immersion test presents a substantial correlation with the LPR measurements and the OCP monitoring of the zones. This correlation has been studied to illustrate the mechanism of corrosion attack within the weld zones. It is proposed that the large initial drop in resistance observed for the weld zones in Figs. 5 and 10 after 1 h of immersion is related to the selective dissolution of the hardening precipitates, thus initiating corrosion attack. Due to the higher concentration of these precipitates in the AA2099 alloy, the initial drop in resistance is much higher compared to the AA2060 alloy. This effect is also seen in the OCP measurements, with a considerable drop in potential after 1 h of immersion, especially for the AA2099 weld zones.

A slight increase in polarisation resistance and OCP is observed as the immersion time progresses. The in-situ micrographs indicate that this increase may be due to the formation of corrosion products that deposit at the mouth of the pits and other sites of anodic activity. However, these corrosion products are porous in nature and are redistributed over time, which then causes attack to resume at the anodic sites. The second drop in resistance for the BM and HAZ regions of both alloys corresponds to the attack on coarse particles within the weld regions, as seen during the immersion test (Figs. 6 and 11). Since these particles are much larger than the hardening precipitates, they are corroded over a longer period of time, as seen by the slower decline in polarisation resistance (Fig. 8 and Fig. 13).

The final drop in resistance, observed only for the AA2060 alloy weld zones, possibly corresponds to the selective dissolution of deformed grains. This is a more gradual attack that stretches for hours, as observed in the LPR measurements in Fig. 8 and also during the immersion test in Fig. 6(a-c). This final drop in resistance is not observed in the AA2099 weld zones. Instead, after 15 h of immersion, the polarisation resistance of the BM and HAZ of AA2099 alloy stabilises till the end of the experiment. The absence of hardening precipitates in the SZ regions allows a more gradual attack, as observed during the immersion tests (Figs. 6c and 11c) and the LPR measurements (Figs. 5d and 10d).

The in-situ immersion test and the surface potential measurements of the entire weld joint reveal that the SZ of the AA2060 is a noticeably unusual region. The SKP measurements after 1 h (Fig. 13b) indicate that attack initiation within the weld joint starts from the AA2060 SZ due to high anodic activity within the region. However, it does not occur in the entire SZ region and instead, only layers that correspond to the alloying elements of the AA2060 alloy are attacked initially. The attack on AA2099 layers within this zone occurs after 3 – 4 h of immersion. It is proposed that the overlapping layers of grains from both alloys in the AA2060 SZ result in a high galvanic activity between them within the region, also observed by Bugarin et al. in their study on dissimilar FSW Al alloys [22]. Due to this, the grains within the SZ tend to corrode preferentially. The deformed grains of the AA2060 alloy within this region are preferentially attacked first (Fig. 6c), whereas the grains of the AA2099 alloy in the SZ corrode later on, as seen in the SKP surface potential map (Fig. 13e).

It is evident that the attack initiation on the weld joint is mainly due to the galvanic coupling within the SZ region. Over time, the other weld zones are attacked due to the galvanic influence between the corroded regions and the initially protected regions. However, after 5 – 6 h of immersion, the attack propagation in each weld zone is due to self-corrosion of the zones. This is also demonstrated in the SKP surface potential plot at 5 h after exposure to NaCl (Fig. 13f), where it is observed that the surface potential has evened out in most regions within both alloys and the difference in surface potential between the weld zones is not sufficient to induce galvanic corrosion between them.

4. Conclusion

The microstructure and corrosion behaviour of the dissimilar friction stir welded AA2060 and AA2099 alloys have been investigated here. The main conclusions are as follows:

- Friction stir welding drastically alters the microstructural features of the weld zones. The AA2060 SZ (weld nugget) forms a banded structure consisting of overlapping layers of grains from both alloys due to the stirring effect of the tool pin.
- The BM of both alloys exhibits highly active behaviour due to the high density of intermetallic particles present.
- The HAZ regions feature similar corrosion behaviour to their respective BM, with slight differences attributed to the reduction in average grain area and the distribution density of intermetallic particles.
- The SZ regions are the most susceptible to attack, with the AA2060 SZ exhibiting two corrosion potentials. This occurs due to the galvanic coupling within the weld nugget caused by the overlapping layers of grains from both alloys.
- The corrosion attack on the entire weld joint is a dynamic process due to the microstructural differences between each weld zone. Attack initiation occurs in the AA2060 SZ due to the galvanic effect within the region.
- The attack initiation for each subsequent zone is determined to be due to the galvanic effect between the zones. In contrast, attack propagation over time is due to self-corrosion of the weld zones in each alloy.

CRediT authorship contribution statement

Vishant Garg: Writing – review & editing, Writing – original draft, Investigation, Formal analysis. **Joost P.B. van Dam:** Writing – review & editing, Validation, Investigation. **Emmanouela Michailidou:** Writing – review & editing, Validation, Supervision, Investigation. **Yaiza Gonzalez-Garcia:** Writing – review & editing, Validation, Supervision, Project administration, Funding acquisition, Conceptualization.

Declaration of Competing Interest

The authors declare that they have no known competing financial interests or personal relationships that could have appeared to influence the work reported in this paper.

Acknowledgements

This study was supported by the European research program Clean Sky 2. The ecoTECH Core Partner project has received funding from the

European Union Horizon 2020 Clean Sky 2 Joint Undertaking under the AIRFRAME ITD grant agreement 945521 and the Transverse Activity ecoDESIGN grant agreement 945549. Egoitz Aldanondo (LORTEK Technological Centre, Basque Research and Technology Alliance (BRTA), Ordizia, Spain) is acknowledged for providing the material.

Appendix A. Supporting information

Supplementary data associated with this article can be found in the online version at doi:10.1016/j.corsci.2024.112519.

Data availability

Data will be made available on request.

References

[1] B. Cai, Z.Q. Zheng, D.Q. He, S.C. Li, H.P. Li, Friction stir weld of 2060 Al-Cu-Li alloy: microstructure and mechanical properties, J. Alloy. Compd. 649 (2015) 19–27, https://doi.org/10.1016/j.jallcom.2015.02.124.
[2] N.D. Alexopoulos, A. Proiou, W. Dietzel, C. Blawert, V. Heitmann, M. Zheludkevich, S.K. Kourkoulis, Mechanical properties degradation of (Al-Cu-Li) 2198 alloy due to corrosion exposure, Procedia Struct. Integr. 2 (2016) 597–603, https://doi.org/10.1016/j.prostr.2016.06.077.
[3] J.V. de Sousa Araujo, U. Donatus, F.M. Queiroz, M. Terada, M.X. Milagre, M.C. de Alencar, I. Costa, On the severe localized corrosion susceptibility of the AA2198-T851 alloy, Corros. Sci. 133 (2018) 132–140, https://doi.org/10.1016/j.corsci.2018.01.028.
[4] P. Rambabu, N.E. Prasad, V.V. Kutumbarao, R.J.H. Wanhill, Chapter 2: Aluminium alloys for aerospace applications, in: N.E. Prasad, R.J.H. Wanhill (Eds.), Aerospace Materials and Material Technologies, 2017: pp. 29–52.
[5] A.E. Hughes, R. Parvizi, M. Forsyth, Microstructure and corrosion of AA2024, Corros. Rev. 33 (2015) 1–30, https://doi.org/10.1515/corrrev-2014-0039.
[6] J.A. DeRose, T. Suter, A. Bałkowiec, J. Michalski, K.J. Kurzydlowski, P. Schmutz, Localised corrosion initiation and microstructural characterisation of an Al 2024 alloy with a higher Cu to Mg ratio, Corros. Sci. 55 (2012) 313–325, https://doi.org/10.1016/j.corsci.2011.10.035.
[7] E.A. Starke, Chapter 1 - Historical Development and Present Status of Aluminum–Lithium Alloys, in: N. Eswara Prasad, A.A. Gokhale, R.J.H. Wanhill (Eds.), Aluminum-Lithium Alloys, Butterworth-Heinemann, Boston, 2014, pp. 3–26, https://doi.org/10.1016/B978-0-12-401698-9.00001-X.
[8] T. Warner, Recently-developed aluminium solutions for aerospace applications: I, Mater. Sci. Forum (2006).
[9] R.J. Rioja, J. Liu, The evolution of Al-Li base products for aerospace and space applications, Met. Mater. Trans. A Phys. Met. Mater. Sci. 43 (2012) 3325–3337, https://doi.org/10.1007/s11661-012-1155-z.
[10] M. Romios, R. Tiraschi, J. Ogren, O. Es-Said, C. Parrish, H. Babel, Design of multistep aging treatments of 2099 (C458) Al-Li alloy, J. Mater. Eng. Perform. 14 (2005) 641–646, https://doi.org/10.1361/105994905X64594.
[11] A. Abd El-Aty, Y. Xu, X. Guo, S.H. Zhang, Y. Ma, D. Chen, Strengthening mechanisms, deformation behavior, and anisotropic mechanical properties of Al-Li alloys: a review, J. Adv. Res 10 (2018) 49–67, https://doi.org/10.1016/j.jare.2017.12.004.
[12] Y. Zhu, G.S. Frankel, Effect of major intermetallic particles on localized corrosion of AA2060-T8, Corrosion 75 (2019) 29–41, https://doi.org/10.5006/2867.
[13] B. Noble, G.E. Thompson, T 1 (Al2CuLi) precipitation in aluminium–copper–lithium alloys, Met. Sci. J. 6 (1972) 167–174, https://doi.org/10.1179/030634572790445975.
[14] U. Donatus, M. Terada, C.R. Ospina, F.M. Queiroz, A. Fatima Santos Bugarin, I. Costa, On the AA2198-T851 alloy microstructure and its correlation with localized corrosion behaviour, Corros. Sci. 131 (2018) 300–309, https://doi.org/10.1016/j.corsci.2017.12.001.
[15] E. Michailidou, P. Visser, J.M.C. Mol, A. Kosari, H. Terryn, K. Baert, Y. Gonzalez-Garcia, The effect of pH on the corrosion protection of aluminum alloys in lithium-carbonate-containing NaCl solutions, Corros. Sci. 210 (2023) 110851, https://doi.org/10.1016/j.corsci.2022.110851.
[16] R.G. Buchheit, J.P. Moran, G.E. Stoner, Electrochemical behavior of the T1 (Al2CuLi) intermetallic compound and its role in localized corrosion of Al-2% Li-3% Cu alloys, Corrosion 50 (1994) 120–130, https://doi.org/10.5006/1.3293500.
[17] S. Cater. Fundamentals of Friction Stir Welding, 3rd Edition, TWI, 2016.
[18] M.Rangel Pacheco, J.Paul Kabche, I. Thesi, F.Nunes Diesel, Temperature distribution analysis in plates joined by Friction Stir Welding. ASME International Mechanical Engineering Congress and Exposition, Proceedings, American Society of Mechanical Engineers (ASME), 2010, pp. 163–169, https://doi.org/10.1115/IMECE2009-12892.
[19] R.S. Mishra, Z.Y. Ma, Friction stir welding and processing, Mater. Sci. Eng.: R: Rep. 50 (2005) 1–78, https://doi.org/10.1016/j.mser.2005.07.001.
[20] V. Proton, J. Alexis, E. Andrieu, C. Blanc, J. Delfosse, L. Lacroix, G. Odemer, Influence of post-welding heat treatment on the corrosion behavior of a 2050-T3 aluminum-copper-lithium alloy friction stir welding joint, J. Electrochem Soc. 158 (2011) C139, https://doi.org/10.1149/1.3562206.
[21] Y.L. Ma, H.Bin Xu, Z.Y. Liang, L. Liu, Corrosion resistance of friction stir welded Al–Cu–Li alloy AA2099-T8, Acta Metall. Sin. (Engl. Lett.) 33 (2020) 127–134, https://doi.org/10.1007/s40195-019-00944-w.
[22] A.F.S. Bugarin, C.P. De Abreu, M. Terada, H.G. De Melo, I. Costa, Effect of friction stir welding (FSW) on the electrochemical behavior and galvanic coupling of AA2024-T3 and AA7475-T651, Mater. Today Commun. 25 (2020) 101591, https://doi.org/10.1016/j.mtcomm.2020.101591.
[23] U. Donatus, B.V.G. de Viveiros, M.C. de Alencar, R.O. Ferreira, M.X. Milagre, I. Costa, Correlation between corrosion resistance, anodic hydrogen evolution and microhardness in friction stir weldment of AA2198 alloy, Mater. Charact. 144 (2018) 99–112, https://doi.org/10.1016/j.matchar.2018.07.004.
[24] G. Rambabu, D. Balaji Naik, C.H. Venkata Rao, K. Srinivasa Rao, G. Madhusudan Reddy, Optimization of friction stir welding parameters for improved corrosion resistance of AA2219 aluminum alloy joints, Def. Technol. 11 (2015) 330–337, https://doi.org/10.1016/j.dt.2015.05.003.
[25] C.V. Rao, G.M. Reddy, K.S. Rao, Microstructure and pitting corrosion resistance of AA2219 Al–Cu alloy friction stir welds – effect of tool profile, Def. Technol. 11 (2015) 123–131, https://doi.org/10.1016/j.dt.2014.10.003.
[26] P. Niu, W. Li, Z. Zhang, X. Yang, Global and local constitutive behaviors of friction stir welded AA2024 joints, J. Mater. Sci. Technol. 33 (2017) 987–990, https://doi.org/10.1016/j.jmst.2017.02.010.
[27] U. Donatus, R.O. Ferreira, N.V.V. Mogili, B.V.G. de Viveiros, M.X. Milagre, I. Costa, Corrosion and anodizing behaviour of friction stir weldment of AA2198-T851 Al-Cu-Li alloy, Mater. Chem. Phys. 219 (2018) 493–511, https://doi.org/10.1016/j.matchemphys.2018.08.053.
[28] U. Donatus, R.M.P.Da Silva, J.V.D.S. Araujo, M.X. Milagre, C.P.De Abreu, C.D.S. C. MacHado, I. Costa, Macro and microgalvanic interactions in friction stir weldment of AA2198-T851 alloy, J. Mater. Res. Technol. 8 (2019) 6209–6222, https://doi.org/10.1016/j.jmrt.2019.10.015.
[29] E. Bousquet, A. Poulon-Quintin, M. Puiggali, O. Devos, M. Touzet, Relationship between microstructure, microhardness and corrosion sensitivity of an AA 2024-T3 friction stir welded joint, Corros. Sci. 53 (2011) 3026–3034, https://doi.org/10.1016/j.corsci.2011.05.049.
[30] V. Proton, J. Alexis, E. Andrieu, J. Delfosse, M.C. Lafont, C. Blanc, Characterisation and understanding of the corrosion behaviour of the nugget in a 2050 aluminium alloy Friction Stir Welding joint, Corros. Sci. 73 (2013) 130–142, https://doi.org/10.1016/j.corsci.2013.04.001.
[31] P. Cavaliere, M. Cabibbo, F. Panella, A. Squillace, 2198 Al-Li plates joined by friction stir welding: mechanical and microstructural behavior, Mater. Des. 30 (2009) 3622–3631, https://doi.org/10.1016/j.matdes.2009.02.021.
[32] A.P. Reynolds, W. Tang, Z. Khandkar, J.A. Khan, K. Lindner, Relationships between weld parameters, hardness distribution and temperature history in alloy 7050 friction stir welds, Sci. Technol. Weld. Join. 10 (2005) 190–199, https://doi.org/10.1179/174329305X37024.
[33] D.A. Wadeson, X. Zhou, G.E. Thompson, P. Skeldon, L.D. Oosterkamp, G. Scamans, Corrosion behaviour of friction stir welded AA7108 T79 aluminium alloy, Corros. Sci. 48 (2006) 887–897, https://doi.org/10.1016/j.corsci.2005.02.020.
[34] J.C.B. Bertoncello, S.M. Manhabosco, L.F.P. Dick, Corrosion study of the friction stir lap joint of AA7050-T76511 on AA2024-T3 using the scanning vibrating electrode technique, Corros. Sci. 94 (2015) 359–367, https://doi.org/10.1016/j.corsci.2015.02.029.
[35] A. Fattah-alhosseini, M. Naseri, D. Gholami, O. Imantalab, F.R. Attarzadeh, M. K. Keshavarz, Microstructure and corrosion characterization of the nugget region in dissimilar friction-stir-welded AA5083 and AA1050, J. Mater. Sci. 54 (2019) 777–790, https://doi.org/10.1007/s10853-018-2820-4.
[36] P. Atz Dick, G.H. Knörnschild, L.F.P. Dick, Anodising and corrosion resistance of AA 7050 friction stir welds, Corros. Sci. 114 (2017) 28–36, https://doi.org/10.1016/j.corsci.2016.10.015.
[37] E. Aldanondo, E. Arruti, A. Echeverria, I. Hurtado, Friction stir welding of lap joints using new Al–Li alloys for stringer-skin joints, Frict. Stir Weld. Process. X (2019) 77–88, https://doi.org/10.1007/978-3-030-05752-7_8.
[38] J. Sullivan, S. Mehraban, J. Elvins, In situ monitoring of the microstructural corrosion mechanisms of zinc-magnesium-aluminium alloys using time lapse microscopy, Corros. Sci. 53 (2011) 2208–2215, https://doi.org/10.1016/j.corsci.2011.02.043.
[39] J.P.B. van Dam, S.T. Abrahami, A. Yilmaz, Y. Gonzalez-Garcia, H. Terryn, J.M. C. Mol, Effect of surface roughness and chemistry on the adhesion and durability of a steel-epoxy adhesive interface, Int. J. Adhes. Adhes. 96 (2020) 102450, https://doi.org/10.1016/j.ijadhadh.2019.102450.
[40] I.A. Kartsonakis, D.A. Dragatogiannis, E.P. Koumoulos, A. Karantonis, C. A. Charitidis, Corrosion behaviour of dissimilar friction stir welded aluminium alloys reinforced with nanoadditives, Mater. Des. 102 (2016) 56–67, https://doi.org/10.1016/j.matdes.2016.04.027.
[41] X. Meng, Z. Xu, Y. Huang, Y. Xie, Y. Wang, L. Wan, Z. Lv, J. Cao, Interface characteristic and tensile property of friction stir lap welding of dissimilar aircraft 2060-T8 and 2099-T83 Al–Li alloys, Int. J. Adv. Manuf. Technol. 94 (2018) 1253–1261, https://doi.org/10.1007/s00170-017-0996-4.
[42] Y. Lin, Z. Zheng, S. Li, X. Kong, Y. Han, Microstructures and properties of 2099 Al-Li alloy, Mater. Charact. 84 (2013) 88–99, https://doi.org/10.1016/j.matchar.2013.07.015.
[43] B. Wang, X.H. Chen, F.S. Pan, J.J. Mao, Y. Fang, Effects of cold rolling and heat treatment on microstructure and mechanical properties of AA 5052 aluminum alloy, Trans. Nonferrous Met. Soc. China (Engl. Ed.) 25 (2015) 2481–2489, https://doi.org/10.1016/S1003-6326(15)63866-3.
[44] V. Proton, J. Alexis, E. Andrieu, J.Ò. Delfosse, A. Deschamps, F. De Geuser, M. C. Lafont, C. Blanc, The influence of artificial ageing on the corrosion behaviour of

a 2050 aluminium-copper-lithium alloy, Corros. Sci. 80 (2014) 494–502, https://doi.org/10.1016/j.corsci.2013.11.060.
[45] Y. Mao, L. Ke, F. Liu, C. Huang, Y. Chen, Q. Liu, Effect of welding parameters on microstructure and mechanical properties of friction stir welded joints of 2060 aluminum lithium alloy, Int. J. Adv. Manuf. Technol. 81 (2015) 1419–1431, https://doi.org/10.1007/s00170-015-7191-2.
[46] Y. Ma, X. Zhou, G.E. Thompson, T. Hashimoto, P. Thomson, M. Fowles, Distribution of intermetallics in an AA 2099-T8 aluminium alloy extrusion, Mater. Chem. Phys. 126 (2011) 46–53, https://doi.org/10.1016/j.matchemphys.2010.12.014.
[47] J. Entringer, M. Meisnar, M. Reimann, C. Blawert, M. Zheludkevich, J.F. dos Santos, The effect of grain boundary precipitates on stress corrosion cracking in a bobbin tool friction stir welded Al-Cu-Li alloy, Mater. Lett.: X 2 (2019) 100014, https://doi.org/10.1016/j.mlblux.2019.100014.
[48] N. Akhtar, H.J. Jin, F. Jia, S.J. Wu, Fatigue crack growth rates in friction stir welding joints of Al-Li 2060-T8X Alloy, Proceedings of 2015 12th International Bhurban Conference on Applied Sciences and Technology (2015) 6–13, https://doi.org/10.1109/IBCAST.2015.7058471.
[49] F. Liu, X. Wang, B. Zhou, C. Huang, F. Lyu, Corrosion resistance of 2060 aluminum-lithium alloy LBW Welds Filled with Al-5.6Cu Wire, Materials 11 (2018), https://doi.org/10.3390/ma11101988.
[50] E. Balducci, L. Ceschini, S. Messieri, S. Wenner, R. Holmestad, Thermal stability of the lightweight 2099 Al-Cu-Li alloy: tensile tests and microstructural investigations after overaging, Mater. Des. 119 (2017) 54–64, https://doi.org/10.1016/j.matdes.2017.01.058.
[51] A.R. Cisko, J.B. Jordon, D.Z. Avery, Z.B. McClelland, T. Liu, T.W. Rushing, L. N. Brewer, P.G. Allison, L. Garcia, Characterization of fatigue behavior of Al-Li alloy 2099, Mater. Charact. 151 (2019) 496–505, https://doi.org/10.1016/j.matchar.2019.03.026.
[52] C.M. MacRae, A.E. Hughes, J.S. Laird, A.M. Glenn, N.C. Wilson, A. Torpy, M. A. Gibson, X. Zhou, N. Birbilis, G.E. Thompson, An examination of the composition and microstructure of coarse intermetallic particles in AA2099-T8, including Li detection, Microsc. Microanal. 24 (2018) 325–341, https://doi.org/10.1017/S1431927618000454.
[53] Y. long Ma, X. rong Zhou, X. min Meng, W. jiu Huang, Y. Liao, X. li Chen, Y. nan Yi, X. xin Zhang, G.E. Thompson, Influence of thermomechanical treatments on localized corrosion susceptibility and propagation mechanism of AA2099 Al–Li alloy, Trans. Nonferrous Met. Soc. China (Engl. Ed.) 26 (2016) 1472–1481, https://doi.org/10.1016/S1003-6326(16)64252-8.
[54] Y. Ma, X. Zhou, W. Huang, G.E. Thompson, X. Zhang, C. Luo, Z. Sun, Localized corrosion in AA2099-T83 aluminum-lithium alloy: the role of intermetallic particles, Mater. Chem. Phys. 161 (2015) 201–210, https://doi.org/10.1016/j.matchemphys.2015.05.037.
[55] M.X. Milagre, U. Donatus, N.V. Mogili, R.M.P. Silva, B.V.G. de Viveiros, V. F. Pereira, R.A. Antunes, C.S.C. Machado, J.V.S. Araujo, I. Costa, Galvanic and asymmetry effects on the local electrochemical behavior of the 2098-T351 alloy welded by friction stir welding, J. Mater. Sci. Technol. 45 (2020) 162–175, https://doi.org/10.1016/j.jmst.2019.11.016.
[56] J.A. Moreto, C.E.B. Marino, W.W. Bose Filho, L.A. Rocha, J.C.S. Fernandes, SVET, SKP and EIS study of the corrosion behaviour of high strength Al and Al-Li alloys used in aircraft fabrication, Corros. Sci. 84 (2014) 30–41, https://doi.org/10.1016/j.corsci.2014.03.001.
[57] Y. Ma, X. Zhou, W. Huang, Y. Liao, X. Chen, X. Zhang, G.E. Thompson, Crystallographic defects induced localised corrosion in AA2099-T8 aluminium alloy, Corros. Eng. Sci. Technol. 50 (2015) 420–424, https://doi.org/10.1179/1743278214Y.0000000237.
[58] J.F. Li, C.X. Li, Z.W. Peng, W.J. Chen, Z.Q. Zheng, Corrosion mechanism associated with T1 and T2 precipitates of Al-Cu-Li alloys in NaCl solution, J. Alloy. Compd. 460 (2008) 688–693, https://doi.org/10.1016/j.jallcom.2007.06.072.
[59] N. Wint, Z.S. Barrett, G. Williams, H.N. McMurray, The study of AA2024 de-alloying using luminol electrogenerated chemiluminescence imaging, J. Electrochem Soc. 166 (2019) C3417–C3430, https://doi.org/10.1149/2.0481911jes.